Master's Thesis

Measurement Device for Magnetic Permeability of Steel in Production Processes

Florian Oberhauser

———————————————

Institute of Electrical Measurement and Measurement Signal Processing
Graz University of Technology
Head of Institute: Univ.-Prof. Dipl.-Ing. Dr.techn. Georg Brasseur

Graz University of Technology

Supervisor: Dipl.-Ing. Dr.techn. Markus Neumayer

Graz, November 17, 2014

Contents

Abstract

The efficiency of electrical machines strongly depends on the magnetic properties (permeability) of the steels providing the main flux guiding path inside the device. Beside this magnetic steels also (ideally) non-magnetic steels are employed regarding mechanical stability issues. The magnetic properties of these steels are crucial for the efficiency of the overall device. In this work a simple measurement device for the determination of the magnetic properties of non-magnetic steels is developed. This work presents a detailed study through existing literature and the development of a novel prototype measurement concept for the determination of the magnetic properties of steels for quality assurance. A detailed study of the presented concept is provided including a user guide for the operation of the developed measurement device. The work provides simulation based studies about the developed device, as well as measurement experiments including measurements using probes out of a real production process. In addition also different variants of the measurement device are explored. The results indicate, that the new measurement device provides good sensitivity with respect to materials with increased permeability.

Zusammenfassung

Der Wirkungsgrad von elektrischen Maschinen wird hauptsächlich durch die magnetischen Eigenschaften der Stähle bestimmt, die den Hauptfluss der Maschine führen. Für die mechanische Stabilität der Maschine werden idealerweise nicht magnetische Stähle verwendet. Die magnetischen Eigenschaften dieser Stähle sind maßgeblichen am Gesamtwirkungsgrad des Geräts beteiligt. In dieser Arbeit wird ein einfaches Gerät zur Bestimmung der magnetischen Eigenschaften von nicht magnetischen Stählen entwickelt. Diese Arbeit präsentiert eine detaillierte Literaturrecherche und die Entwicklung eines neuartigen Konzepts eines Messgeräte zur Bestimmung der magnetischen Eigenschaften von nicht magnetischem Stahl für die Qualitätssicherung. Eine detaillierte Untersuchung des Konzepts inklusive einer Gebrauchsanweisung zum Betrieb des Geräts wird zur Verfügung gestellt. Des weiteren präsentiert die Arbeit auf Simulationen basierende Studien zum entworfenen Gerät und Messexperimente unter Verwendung von Proben aus dem Herstellungsprozess. Zusätzlich wurden noch unterschiedliche Varianten des Messgeräts untersucht. Die Ergebnisse zeigen, dass das entwickelte Messgerät eine gute Sensitivität in Bezug auf Materialien mit erhöhten magnetischen Permeabilitäten hat.

Statutory Declaration

I declare that I have authored this thesis independently, that I have not used other than the declared sources / resources, and that I have explicitly marked all material which has been quoted either literally or by content from the used sources.

Eidesstattliche Erklärung

Ich erkläre an Eides statt, dass ich die vorliegende Arbeit selbstständig verfasst, andere als die angegebenen Quellen/Hilfsmittel nicht benutzt und die den benutzten Quellen wörtlich und inhaltlich entnommene Stellen als solche kenntlich gemacht habe.

_____   _____   _____
Ort   Datum   Unterschrift

1 Introduction

In the construction process of electro magnetic devices different types of steels are used. Steels with a high magnetic permeability μ_r are used to guide the magnetic flux along defined paths. Examples are the yoke of a transformer made from steel sheets or the rotor and stator in electric motors. Steels with a low relative permeability μ_r, ($\mu_r = 1$ ideal case) are usually used to fasten and secure the mechanical construction. Examples are the housing of transformers or the stator clamping plate of an electric motor as depicted in Fig. 1.1.
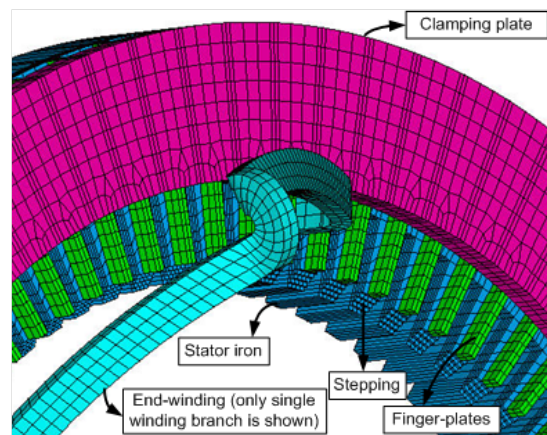
Fig. 1.1: Stator of an electro motor with non magnetic fixing parts. The clamping plate and finger plates which fix the stator iron are usually made of non magnetic steel.

One of this used feebly magnetic steels is the steel 1.4301[1] with nominal specified relative magnetic permeability μ_r of less then 1.3. Due to production diversification the relative magnetic permeability can differ significantly from the specified one. The impact of this deviation can be recognized when a 100 g feebly magnetic steel block with a relative permeability of less than 2.5 can be lifted using of a permanent magnet. A picture of a non magnetic steel block with such a high deviation in the relative permeability is presented in Fig. 1.2. With respect to the high permeability in the magnetic path, even a small increase in the permeability has a large impact on the efficiency of the device due to its non linear behavior. The higher the deviation of the relative permeability of the non magnetic steel the higher the additional electric losses. Electric losses reduce the

efficiency of the electric machine and also contribute to the warming of the machine.

Fig. 1.2: Non magnetic steel sample with $\mu_r \leq 2.5$ lifted up by a permanent magnet.

To prevent the use of non magnetic steels with a high deviation in the relative permeability a quality inspection has to be done. Most available gaugs need material samples with a special shape for measurement. An easy and fast, but uncertain method for a quality inspection is the use of a permanent magnet. The permanent magnet is attached to the surface of a vertical upright positioned steel sample. If the attraction force is small the permanent magnet slips down along the surface. Depending on the speed the material sample is categorized as non-, low- or medium magnetic. If the permanent magnet does not move, the steel sample is categorized as high magnetic. The categorization, which use the permanent magnet is highly affected by the surface parameters of the steel sample and the subjective perception of the person who performs the test. The outcome of this works should be a gauge which can categorize the steel samples with a higher resolution and a better repeatability. In addition the gauge should be used to estimate the relative permeability of the material sample under test. The categorization can be done on defined thresholds and or reference materials.

This work presents the development of a measurement device to determine the relative permeability of feebly magnetic materials. In Sec. 1.1 an overview of already known methods to determine the relative permeability of materials is presented. The results of the review and the outline of the work are presented in Sec. 1.2.

1.1 Review of Existing Methods

This sections gives an outline of the state of the art possibilities to determine the permeability of materials in particular non magnetic steels. The approaches can be grouped according to the measurement principle. First, guided methods rely on a closed magnetic circuit were the magnetic flux of a measurement setup is influenced by a material sample. Second, unguided methods use magnets or coils and determine the change in the magnetic field in free space. Finally, there are several approaches which measure the resulting force between a material sample and the measurement device. The American Society for Testing and Material (ASTM) International has established several standard procedures which fall in the three mentioned categories.

The existing methods get rated according to their measuring range instead of their accuracy because for most methods no accuracy is stated and the requirements are determined with respect on the material sample shape geometry.

A well established guided measurement approach to characterize materials with low permeability is presented by Grouber [2]. The discussed device consists of a magnetic circuit connected to a flux measuring coil and an electronic integrator as illustrated in Fig. 1.3. The magnetic circuit comprises a permanent magnet with a wire coil and an air gap for the insertion of the sample material. As soon as the sample material is inserted into the magnetic circuit, the flux changes and a voltage is induced. The induced voltage is then fed to an integrator circuit whose output voltage gives a measure for the magnetic permeability of the material sample.
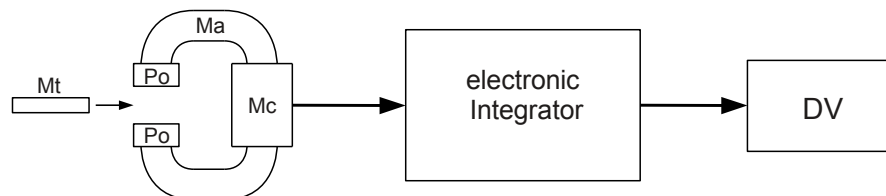
Fig. 1.3: Illustration of guided setup [2]. Legend: Ma ...permanent magnet; Po ...soft iron pole pieces; Mc ...measuring coil; Mt ...material to be tested; DV ...digital voltmeter.

Whereas the structure of the presented approach is relatively simple, it requires an exact calibration with known materials and a highly stable integrator circuit.

Another guided approach to determine the relative permeability using a ring coil and a special waveform is presented by Woo *et al.* Fig. 1.4 shows a block diagram of the

measurement setup and the involved circuitry. In contrast to methods using only DC fields, this approach has the advantages that the material sample is stationary during the measurement and that the drift and the input impedance loading effect can be avoided. The disadvantages are the higher complexity to generate the special waveform and the requirements regarding the sample geometry.
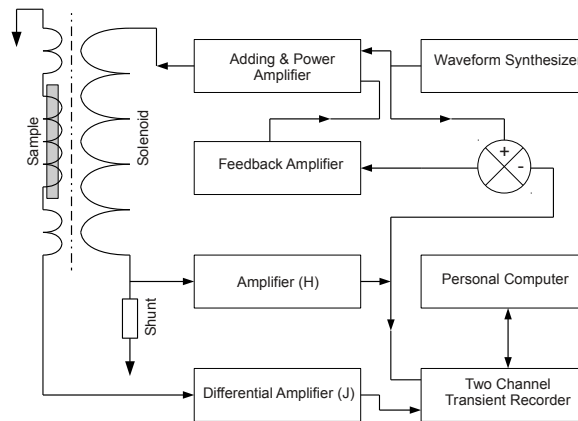
Fig. 1.4: Signal generation and measurement setup [3]. Solenoid with material sample under test. Signal generation and measurement blocks.

Unguided measurement systems [4] typically use a cylindrical permanent magnet with a defined distance to the sample material as shown in Fig. 1.5. The changes to the magnetic field caused by the presence of the sample material are measured using magnetic field sensors. This approach is used for example in a commercially available system by FOERSTER [5]. The nonlinear nature of the sensor principle limits the measurement range for the relative permeability of the testing material to a value of $\mu_r = 4$.
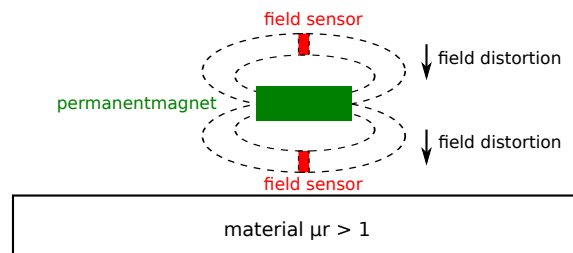
Fig. 1.5: The principle of measurement shows the cylindrical permanent magnet, the field sensors above and below the magnet and the certain flux lines.

A popular unguided approach to characterize the properties of magnetic materials is based on eddy current measurements and is therefore referred to as *Eddy Current Testing*. This principle allows for the measurement of the conductivity as well as the permeability and can be carried out using different signal wave forms [6, 7]. Although these measurements are more versatile in the sense that they also provide the conductivity, the disadvantage is that the measurement setup is relatively complex and that the measured permeability shows a high dependency on the geometric setup and the material conductivity.

Alternative concepts, for example the work presented by Davis [8] measure the resulting force between a permanent magnet and a material sample. In particular, the force is determined using a highly sensitive micro balance scale as depicted in Fig. 1.6. For cylindrical material samples, the author discusses an analytic relation between the relative permeability and the resulting force. However, the major limitation of this approach, however is the limited measurement range resulting from the nonlinear behavior.
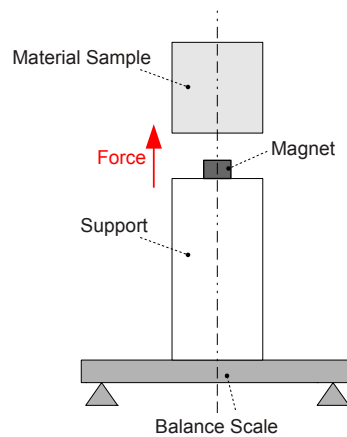
Fig. 1.6: The principle measurement [8] shows the magnet on the top of the support with above placed material sample.

1.1.1 Standardized Measurement Methods

Due to the importance and complexity of permeability measurements, standardized concepts have been proposed by the American Society for Testing and Materials International to allow for reproducible and accurate measurements. The standards determine the underlying measurement principle (guided, unguided or force measurement), geometric setup and the electrical properties. Furthermore, the specific measurement ranges are described which provides a guideline to choose a particular measurement setup for a given application.

The ASTM standard A341/A341M-00 [9] falls in the category guided method, is comparable to the ATSM standards A342/A342M-99 test method 1 and A596/A596M–95. The main difference is the separate magnetic field strength sensing coil. The basic circuit is shown in Fig. 1.7.
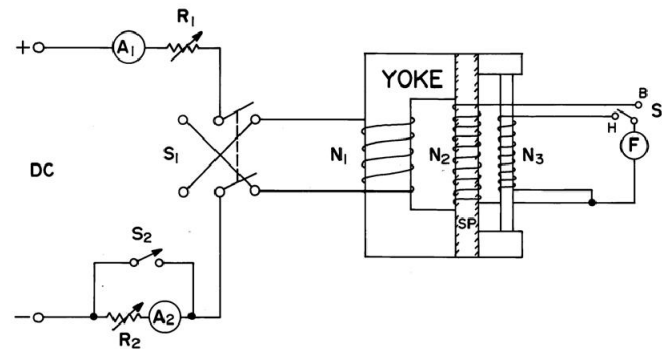
Fig. 1.7: ASTM A41/A341M–00 basic circuit [9], Legend: A_1-Am meter, A_2-Ammeter, B-Flux Density Test Position, F-Fluxmeter, H-Magnetic Field Strength Test Position, N_1-Magnetizing Coil, N_2-Flux Sensing Coil,N_3-Magnetic Field Strength Sensing Coil, R_1-Rheostat, R_2-Rheostat, S_1-Reversing Switch, S_2-Hysteresis Control Switch, S_3-Fluxmeter Selecting Switch, SP-Specimen.

The ASTM standard A342/A342M-99 [10] includes three methods to determine the permeability of a material:

- The first test method presented in Fig. 1.8 falls in the category guided methods and is applicable up to a relative permeability of $\mu_r = 4.0$. The sample material is inserted in the test coil and the magnetic field strength is adjusted to the desired value. Then the magnetizing current is reversed and the value of the fluxmeter gives the permeability of the sample material.

- The second test method illustrated in Fig. 1.9 falls in the category force methods and is applicable up to a relative permeability of 1.05. The sample material has to be longer than 66mm and shall not exceed a width of 12.7mm. The sample material is placed on a balance and inserted at the center line of a specific electromagnet. To measure the weight of the sample the current is set to zero. Then the current of the electromagnet is switched on and the magnet field strength is adjusted to 40 kA/m. The current is reversed a few times to nullify the effect of hysteresis in the electromagnet core and then the weight of the sample is measured with magnetizing current on. The weight difference gives a measure for the permeability of the sample material.

- The third test method shown in Fig. 1.10 falls in the category force method and is applicable up to a relative permeability at the same value as a calibrated reference

material. The reference material is inserted in a defined holding position on the device and the permanent magnet is attached to the reference material by a force depending on the permeability of the reference material. The device is placed on the sample material and if the permeability of the sample material is higher than the permeability of the reference material the permanent magnet will break the contact with the reference material and vice versa. By changing the reference materials it's possible to bracket the permeability of the sample material.
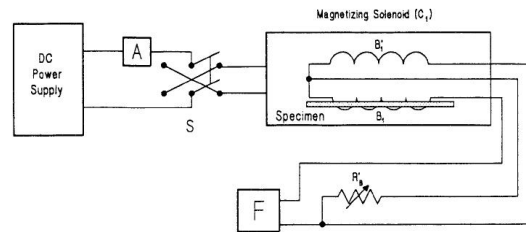
Fig. 1.8: ASTM A342/A342M-99 1. test method [10], Legend: S-Current Reversing Switch, A- Ammeter, F-Fluxmeter, C_1-Magnetizing Solenoid, B_1-Test Coil, B_1'-Compensating Coil, R_S'-Air Flux Compensating Resistor.
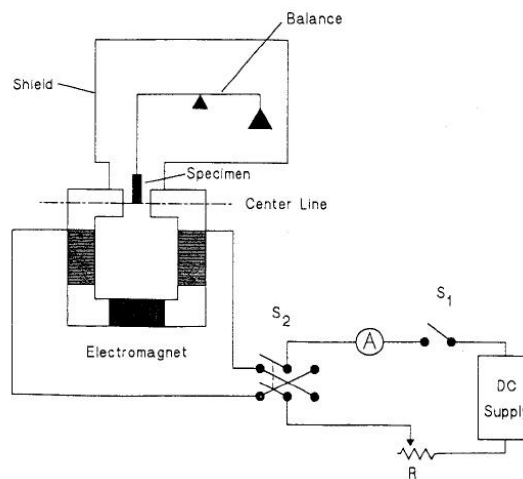
Fig. 1.9: ASTM A342/A342M-99 2. test method [10], Legend: S_1-SPST Switch, S_2-Reversing Switch, A-Ammeter, R-Rheostat.
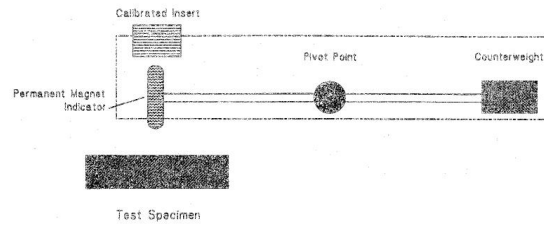
Fig. 1.10: ASTM A342/A342M-99 3. test method [10].

The ASTM standard A343-97 [11] is a guided method and determines the permeability and the magnetic losses. For this purpose, the sample material needs to form a quadratic test frame **(Epstein Test Frame)** with a side length of 250 mm to which coils are applied. With the resulting reference transformer (see Fig. 1.11), a defined measurement run can be performed to determine the individual material parameters.
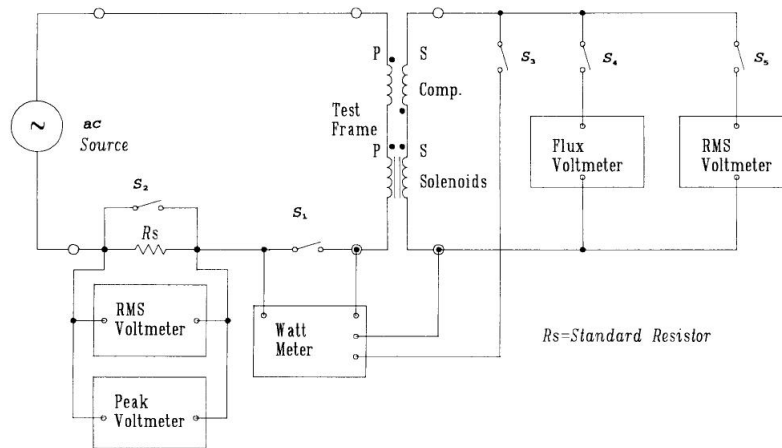
Fig. 1.11: ASTM A343-97 basic circuit [11].

The ASTM standard A596/A596M–95 [12] is a guided method to determine the DC permeability of a material. A test ring is constructed from the sample material which is equipped with a primary and secondary coil. The basic circuit is shown in Fig. 1.12. Similar to the Epstein Test Frame, the permeability can be determined by a applying a standard measurement procedure.
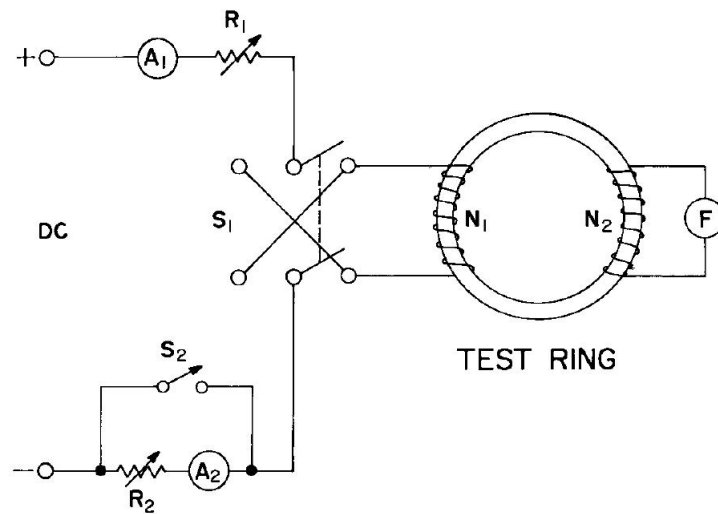
Fig. 1.12: ASTM A596/A596M–95 basic circuit [12], Legend: A_1-Ammeter, A_2-Ammeter, N_1-Primary Winding, N_2-Secondary Winding, F-Fluxmeter, R_1-Rheostat, R_2-Rheostat, S_1-Reversing Switch, S_2-Hysteresis Control Switch.

1.1.2 Conclusion

Although there exists a wide variety of measurement principle to determine the magnetic permeability, most systems show several drawbacks regarding requirements on the size and shape of the material samples and the achievable measurement range. As a result, the existing approaches have limitations with respect to their usage in production processes. Guided measurement approaches require a relatively simple setup and are robust to environmental influences which make them promising for the use in production processes. The challenge of a varying sample geometry can be overcome by a generalized magnetic circuit design which provides a higher flexibility.

1.2 Generalized Guided Measurement Principle

The idea for a flexible permeability measurement system is to use an U-shaped core consisting of a highly permeable steel as shown in Fig. 1.13. The concept is suitable for material samples with different dimensions and only requires a flat surface. The applied coil introduces a magnetic field which depends on the permeability of the material sample. The U-shaped core features an air gap, which accommodates a B-Field sensor to measure the changes in the magnetic field. By employing a reference measurement and an advanced calibration strategy, the measured B-field changes can be used to determine the material permeability.
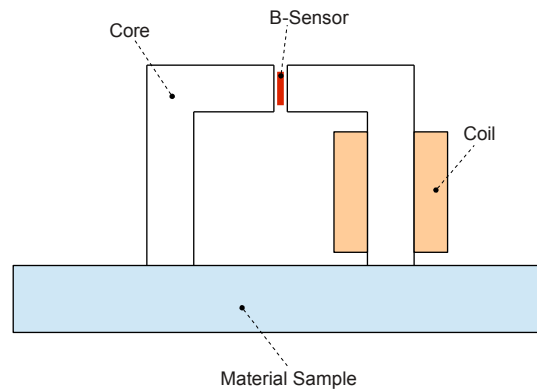
Fig. 1.13: Initial concept idea. The concept consists of a high magnetic steal core with an air gap. A B-field sensor inside the air gap and the magnetization coil.

Starting from the generalized measurement principle described above, several specific geometric setups with different stray field characteristics are analyzed and evaluated in a series of simulations and measurements. The remainder of this work is structured into three chapters as described below.

- Chapter 2: Theory, Modeling and Simulation of Magnetic Circuits

    In the first part of the chapter the used simulation module is presented. Next the magnetic circuit theory as an analytic access to determine the relative permeability of a material is evaluated and verified by simulations. At last an introduction to the FEM-simulation, the setup of an configurable simulation model and an evaluation on the standard quality inspection is given.

- Chapter 3: Permeability Sensor Design

    The initial part of the chapter is the discussion of the three developed design concepts. Followed by the prototype specification with subsequent magnetic parameter design and a thermal design analysis. At last the electronic circuits for the Hall sensor are developed and a material reference measurement is presented.

- Chapter 4: Prototype Verification and Measurements

    The chapter presents the automated test setup followed by a calibration specification depending on a known magnetic circuit. With the calibrated system the different design concepts are compared with each other. Next, different measure-

ments on the thickness dependency, statistical behavior, sensitivity to a non flat surface and orientation influence of samples are reviewed in detail. Based on this measurements a number of material samples are measured followed by a relative magnetic permeability estimation for each sample.

2 Theory, Modeling and Simulation of Magnetic Circuits

This chapter presents the modeling of a sensor system with a prevalent use of a simulation tool. As initial base the concept idea in Chapter 1 is used. In order to create a realistic sensor model some knowledge about the material samples is needed. A short introduction describes the important simulation modules used in the modeling process. Based on the results of the simulation an equivalent magnetic circuit model is defined. The possibility to estimate the relative permeability with the equivalent model is tested. As input to the equivalent model the sensor values from the simulation are used. Then the currently used quality inspection based on the attraction force of a permanent magnet is inspected in more detail. This test method used in the quality control has been presented in Chapter 1.

The simulations are done on the **Comsol Multiphysics AC/DC Module** where further the magneto static is used. The main equations used by this module can be found in the Comsol Reference Manual [13].

2.1 Magnetic Equivalent Circuit

The idea of the magnetic equivalent circuit is to replace the components within a magnetic circuit by concentrated components, such as in network theory. The equivalent circuit in Fig. 2.1b replaces the different sections of the magnetic circuit in Fig. 2.1a with concentrated network elements. The equivalent circuit replaces the magnetic reluctances for the two identical core halves with $R_{\mathrm{Core,S1}}$ and $R_{\mathrm{Core,S2}}$, the air gap with R_{Gap}, the material sample with R_{Mat} and the magnetic voltage source with the magnetomotive force Θ.
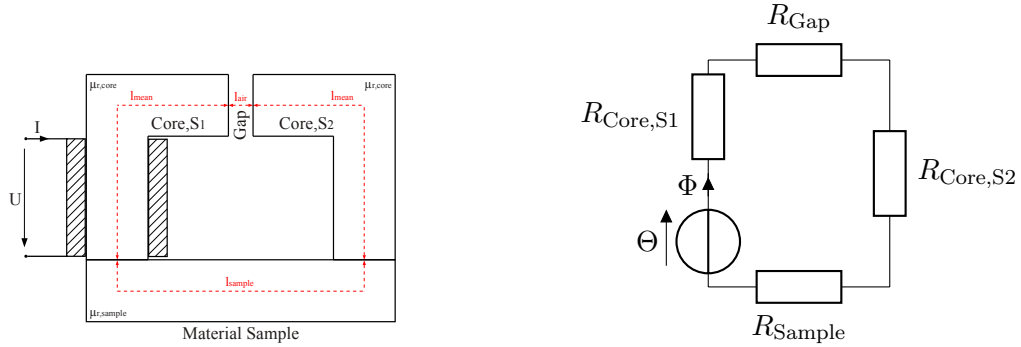
(a) Physical model with mean path length, magneti-
zation source and different materials.

(b) Magnetic equivalent circuit to the pysical
model.

Fig. 2.1: Pysical model and magnetic equivalent circuit.

2.1.1 Analytic Analysis

In most cases the magnetic circuit consists of serial concentrated elements which form
the different sections e.g. excitation coil, air gaps and metal section with different
cross areas and or material parameters. By comparing the concentrated elements of the
magnetic equivalent circuit with the electric circuit a lot of analogical equation as e.g.
the magnetic flux Φ and the electric current I can be found. The analogies are only
formally and listed in Tab. 2.1.

elec. Parameter	Symbol	magn. Parameter	Symbol
elec. Voltage	U	magn. Voltage	V_m
elec. Current	I	magn. Flux	Φ
elec. Resistance	R	magn. Reluctance	R_m
elec. Conductivity	γ	magn. Permeability	μ
elec. Current Density	J	magn. Flux Density	B_m
elec. Field	E	magn. Field	H
Cross Section	A	Cross Section	A
Length	l	Length	l

Tab. 2.1: Analogy of electric and magnetic parameters.

Equ. (2.1) to Equ. 2.5 describe how the different sections and parameters of the magnetic

circuit have to be considered in order to get concentrated network elements.

$$\Theta = N \cdot I = \sum H \cdot l = \sum V_m \qquad\qquad [\Theta] = A \qquad (2.1)$$

$$V_m = H \cdot l \qquad\qquad [V_m] = A \qquad (2.2)$$

$$\Phi = B \cdot A = \frac{V_m}{R_m} \qquad\qquad [\Phi] = T \cdot m^2 = Vs = Wb \qquad (2.3)$$

$$R_m = \frac{l}{\mu_0 \cdot \mu_r \cdot A} \qquad\qquad [R_m] = \frac{A}{Vs} \qquad (2.4)$$

$$\mu = \frac{B}{H} \qquad\qquad [\mu] = \frac{H}{m} = \frac{Vs}{Am} \qquad (2.5)$$

If a stray flux and or a core fill factor have to be considered Equ. (2.6) and Equ. (2.7) are relevant. In Tab. 2.2 the used expressions are listed.

$$\theta_{st} = \sigma \cdot \theta \qquad\qquad [\theta_{st}] = A \qquad (2.6)$$

$$k_e = \frac{A_{met}}{A} \qquad\qquad [k_e] = 1 \qquad (2.7)$$

Parameter Name	Symbol
Stray Flux	θ_{st}
Stray Factor	σ
Metal Fill Factor	k
Metal Cross Section	A_{met}

Tab. 2.2: Additional parameters used in the magnetic circuit theory.

With Equ. (2.8) the relative magnetic permeability of a material sample can be calculated from the measured magnetic flux density B_{Gap} in the air gap. This equation is only valid for the magnetic equivalent circuit in Fig. 2.1b.

$$\mu_{r,sample} = \frac{l_{sample} \cdot B_{Gap} \cdot A_{Core}}{\mu_0 \cdot A_{sample} \cdot (\Theta \cdot \sigma - B_{Gap} \cdot A_{Core} \cdot R_{Core,ges})} \qquad (2.8)$$

2.1.2 Equivalent Magnetic Circuit Calculation

An initial calculation is done on a magnetic circuit with its parameters listed in Tab. 2.3.

Parameter Name	Symbol	Value
Mean Core Path Length	l_{mean}	41 mm
Mean Sample Path Length	l_{sample}	40 mm
Mean Air Gap Length	l_{gap}	1 mm
Magnetization Current	I	1 A
Coil Turns	N	925
Core Cross Section	A_{core}	$(10\,\mathrm{mm})^2$
Core Relative Permeability	$\mu_{\mathrm{r,core}}$	5000
Sample Relative Permeability	$\mu_{\mathrm{r,sample}}$	$1\ldots 25$

Tab. 2.3: Magnetic circuit parameters.

The calculation is done with the values listed in Tab. 2.3 and the values from Equ. (2.18) and Equ. (2.19). The relative permeability of the material is chosen with $\mu_{\mathrm{r,sample}} = 3$.

$$\Theta = N \cdot I \cdot (1 - \sigma_{\mathrm{st,coil}}) \cdot (1 - \sigma_{\mathrm{st,gap}}) = 925 \cdot 1\,\mathrm{A} \cdot 0.63 \cdot 0.85 = 495\,\mathrm{A} \tag{2.9}$$

$$R_{\mathrm{core,S1}} = R_{\mathrm{core,S2}} = \frac{l_{\mathrm{mean}}}{\mu_0 \cdot \mu_{\mathrm{r,core}} \cdot A_{\mathrm{core}}} = \frac{0.041\,\mathrm{m}}{4\pi \cdot 10^{-7}\,\mathrm{Vs/Am} \cdot 5000 \cdot (10\,\mathrm{mm})^2} \tag{2.10}$$

$$R_{\mathrm{core,S1}} = R_{\mathrm{core,S2}} = 65253\,\mathrm{H}^{-1} \tag{2.11}$$

$$R_{\mathrm{air}} = \frac{l_{\mathrm{air}}}{\mu_0 \cdot A_{\mathrm{core}}} = \frac{0.001\,\mathrm{m}}{4\pi \cdot 10^{-7}\,\mathrm{Vs/Am} \cdot (10\,\mathrm{mm})^2} = 7957747\,\mathrm{H}^{-1} \tag{2.12}$$

$$R_{\mathrm{mat}} = \frac{l_{\mathrm{sample}}}{\mu_0 \cdot \mu_{\mathrm{r,sample}} \cdot A_{\mathrm{sample}}} = \frac{0.04\,\mathrm{m}}{4\pi \cdot 10^{-7}\,\mathrm{Vs/Am} \cdot 3 \cdot (10\,\mathrm{mm})^2} \tag{2.13}$$

$$= 106103295\,\mathrm{H}^{-1} \tag{2.14}$$

$$\Phi_{\mathrm{tot}} = \frac{\Theta}{R_{\mathrm{m}}} = \frac{\Theta}{R_{\mathrm{core,S1}} + R_{\mathrm{core,S2}} + R_{\mathrm{air}} + R_{\mathrm{sample}}} = \frac{495\,\mathrm{A}}{114191549\,\mathrm{H}^{-1}} \tag{2.15}$$

$$= 4.34 \cdot 10^{-6}\,\mathrm{Wb} \tag{2.16}$$

$$B_{\mathrm{air}} = \frac{\Phi_{\mathrm{tot}} \cdot \sigma_{\mathrm{eff}}}{A_{\mathrm{core}}} = \frac{4.34 \cdot 10^{-6}\,\mathrm{Wb}}{(10\,\mathrm{mm})^2} = 43.3\,\mathrm{mT} \tag{2.17}$$

2.2 FEM Simulation

In this section a comparison of the equivalent magnetic circuit model and a numeric 3D simulation model is done. The equivalent magnetic circuit model can be used to calculate the relative permeability of the material sample from the measured Hall sensor values in the air gap. A simulation is done based on the parameters listed in Tab. 2.3. In the simulation model the magnetic flux density is calculated at specific points which are indicated in Fig. 2.2. The resulting values are used to calculate the stray field at the coils and at the air gap as indication to the equivalent magnetic circuit model.
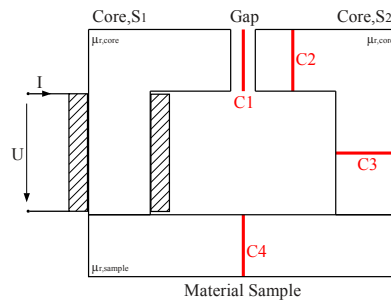
Fig. 2.2: Physical model with indicated magnetic flux density B calculation areas.

In Tab. 2.4 the simulation values at the defined cross sections are listed.

Sample Relative Permeability	Cross Sections Flux Density			
$\mu_{\mathrm{r,sample}}$	B_{C1}	B_{C2}	B_{C3}	B_{C4}
-	T	T	T	T
1.000	0.288	0.340	0.530	0.021
3.000	0.312	0.369	0.587	0.054
5.000	0.331	0.391	0.629	0.082
7.000	0.347	0.409	0.666	0.108
9.000	0.361	0.426	0.699	0.132
11.000	0.374	0.442	0.729	0.155
13.000	0.387	0.457	0.757	0.177
15.000	0.399	0.471	0.783	0.199
17.000	0.410	0.484	0.763	0.219
19.000	0.420	0.496	0.788	0.239
21.000	0.431	0.509	0.812	0.258
23.000	0.441	0.520	0.835	0.277
25.000	0.450	0.532	0.858	0.295

Tab. 2.4: Magnetic flux density at the indicated cross sections.
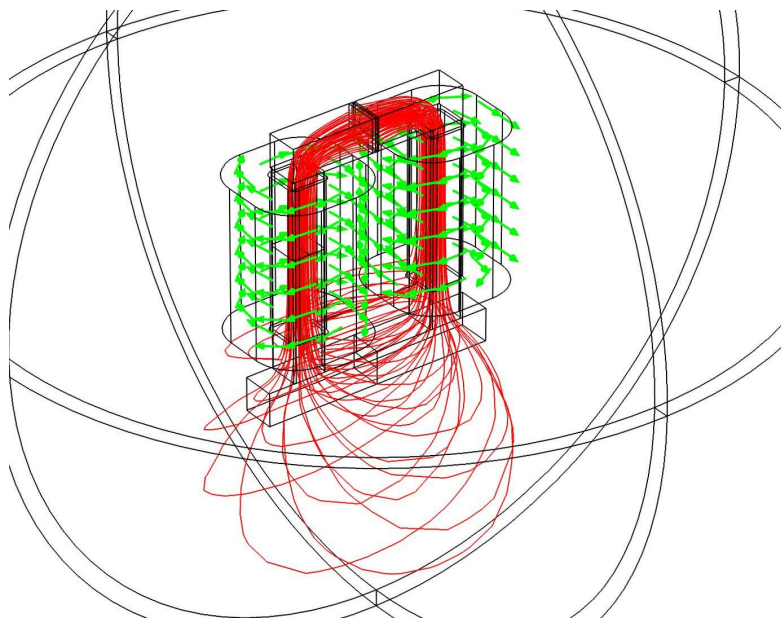
Fig. 2.3: Initial configurable 3D simulation model with flux lines and coil winding direction.

The calculation of the mean value of the stray field at the coil and the air gap is done in Equ. (2.18) and Equ. (2.19). The calculated stray field values are high because the material sample has a low relative permeability.

$$\sigma_{\text{st,coil}} = 1 - \frac{\bar{B}_{\text{C2}}}{\bar{B}_{\text{C3}}} = 1 - \frac{0.361}{0.572} = 0.37 \tag{2.18}$$

$$\sigma_{\text{st,gap}} = 1 - \frac{\bar{B}_{\text{C1}}}{\bar{B}_{\text{C2}}} = 1 - \frac{0.306}{0.361} = 0.15 \tag{2.19}$$

The magnetic equivalent circuit defined in Sec. 2.1 is compared with the results for some geometry simulation model.
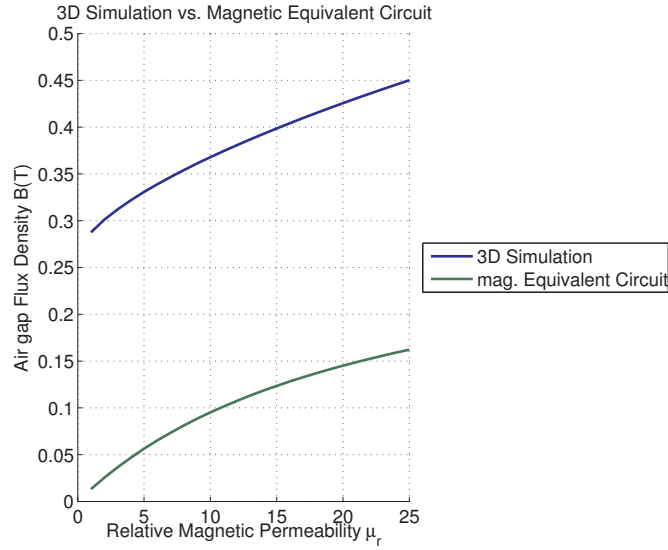
Fig. 2.4: Magnetic equivalent circuit vs. 3D simulation. The figure shows the results of the magnetic equivalent circuit model compared with the 3D Simulation.

The comparison between the simulation and the calculation results in Fig. 2.4 show a significant difference but similar trends. A reason for the high difference is that the magnetic circuit theory depends on the knowledge of the cross sections where the magnetic field is mainly present. For materials with a low magnetic permeability the area of the magnetic field is not restricted to the cross section of the material. The numerical validation shows that the equivalent magnetic circuit is not a good choice to describe this kind of magnetic circuit.

2.3 Experimental Evaluation of the Standard Quality Inspection Approach

In this section the quality inspection of low magnetic materials with a permanent magnet is inspected in more detail. On this purpose the possibility to evaluate the relative magnetic permeability of a material sample by measuring the attraction force of a permanent magnet to the sample is evaluated. This alternative method has been described in the related work in Sec. 1.1. The simulation gives an idea about the dimension of the magnetic force depending on the relative permeability of a material. The results from the simulation are verified by real measurements.

The simulation in Fig. 2.5a uses the geometric dimensions of the material samples from Sec. 3.6 and is done for different permanent magnet remanences B_r and different relative permeabilities μ_r of the sample material illustrated in Fig. 2.5b. The magnetic remanence

for the simulation varies between $B_r = 1.3 \ldots 1.4$ T and the relative permeability $\mu_r = 1 \ldots 3$.

(a) Geometric dimensions of the setup and $norm(\mathbf{B})$ in Tesla indicated as color bar.

(b) Attraction force against the relative permeability at different remanences.
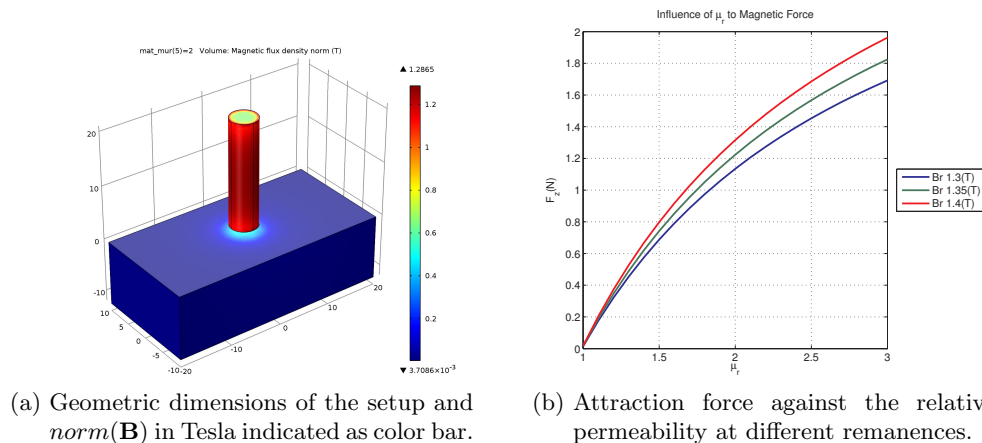
Fig. 2.5: The magnetic force simulation with geometric setup and the resulting force against the relative permeability at different permanent magnet remanences.

Force	Remanenz B_r		
N	T		
	1.3	1.35	1.4
$\mu_r = 1.000$	0.015	0.016	0.017
$\mu_r = 1.200$	0.321	0.346	0.373
$\mu_r = 1.400$	0.576	0.621	0.668
$\mu_r = 1.600$	0.791	0.853	0.917
$\mu_r = 1.800$	0.975	1.052	1.131
$\mu_r = 2.000$	1.135	1.224	1.316
$\mu_r = 2.200$	1.274	1.374	1.478
$\mu_r = 2.400$	1.397	1.507	1.620
$\mu_r = 2.600$	1.506	1.624	1.747
$\mu_r = 2.800$	1.604	1.730	1.860
$\mu_r = 3.000$	1.692	1.825	1.962

Tab. 2.5: Magnetic force simulation results.

The simulation results demonstrate that a permanent magnet with a high remanence can generate large forces even at small relative permeabilities. But as depicted in Fig. 2.5b the results show a saturation effect. This saturation effect makes the measurement concept insensitive to material samples with a high relative permeability.

The measurement is made with a NDFEB permanent magnet with a remanent flux

density of about $1.33\ldots1.37$ T, the material samples from the BH-measurement from Sec. 3.6 and a balance scale. The measurement setup is illustrated in Fig. 2.6a. The values from the balance scale are converted into a force. As presented in Fig. 2.6b with the calculated force value the related relative magnetic permeability can be looked up from the force simulation results. In Tab. 2.6 the measurement results are listed.

Sample	B_r	Measured Balance Scales Value	Calculated Force	Looked Up μ_r
	T	g	N	-
low	1.33	9	0.088	1.04
medium	1.33	27	0.265	1.15
high	1.33	146	1.43	2.35

Tab. 2.6: Magnetic force measurements.

(a) Sketch of the force measurment setup with balance scale and permanent magent.

(b) Attraction force depending on the relative permeability at a remanence of 1.33 T and force measurement results.
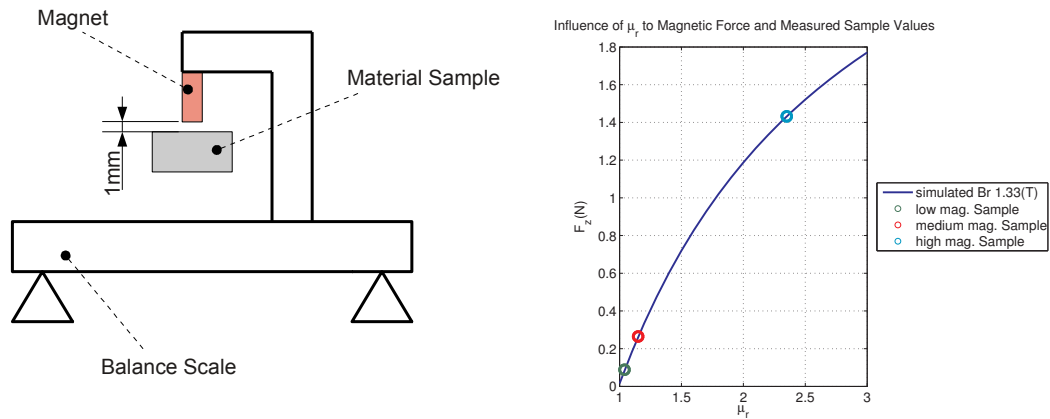
Fig. 2.6: In Fig. 2.6a a sketch of the force measurement setup is shown. In Fig. 2.6b the measured forces are plotted into the simulations results.

The results in Fig. 2.6b present, that a permeability measurement on basis of the attraction force between a material sample and a permanent magnet gives a good reference to the actual relative permeability. The looked up relative permeability values in Tab. 2.6 and the start values from the BH-Curves in Fig. 3.7b are well comparable. Additionally it can be seen that even small relative permeabilities can lead to high attraction forces at high magnetic fields.

3 Permeability Sensor Design

This chapter presents the design of a sensor for permeability measurements. First, different design concepts and their gain with respect to the initial design are discussed. Second, the designs run through different states in order to specify the dimensions and the magnetization coils with a thermal survey based on a set of given design parameters. Third, the electronic circuits for the sensor are elaborated and dimensioned. Finally, the BH-curves of a selected amount of material samples are measured at the *University of Graz Physical Institute*. This measurement results are used in the simulations and as reference materials.

3.1 Discussion of Design

Based on the measurement principle outlined in Chapter 1, the purpose of this chapter is to develop a specific sensor design for permeability measurement. In order to develop a solution, which is robust against the influence of magnetic stray fields, three prototype setups are designed, simulated and analyzed in a series of measurements.

Fig. 3.1a sketches the scheme of the first prototype, which uses two magnetization coils to generate a symmetric field. The targeted low permeability of the measurement samples potentially lead to a considerable stray field as indicated by the schematic field lines in Fig. 3.1a. For this purpose the Prototypes B and C use an additional U-shaped core to minimize unwanted stray fields. Changing the current direction in the magnetization coils results in the magnetic field characteristics as shown in Fig. 3.1b and 3.1c, respectively. In particular, Prototype B uses a magnetic field perpendicular to the material sample whereas Prototype C uses a tangential one.

(a) Prototype A

(b) Prototype B (perpendicular)

(c) Prototype C (tangential)
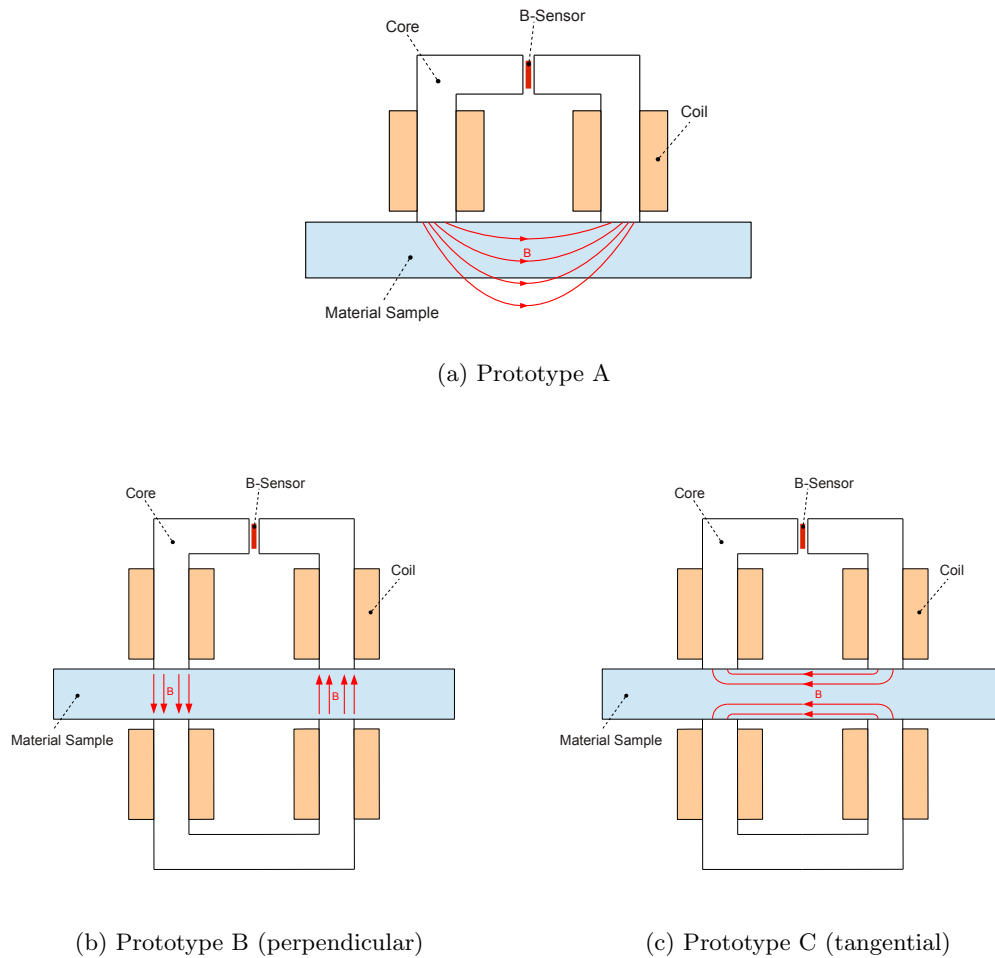
Fig. 3.1: Prototype A uses a U-shaped core with two magnetization coils to establish a symmetric magnetic field. Prototypes B and C use a second U-shaped core and different current directions to establish a perpendicular and tangential magnetic field, respectively.

All three prototypes use a B-field sensor in the air gap to measure changes in the magnetic field depending on the presence of a material sample. The B-field sensor is a Hall Sensor which provides an output voltage proportional to the magnetic field over a large range $(0 \ldots 2 \text{ T})$. The sensor requires a highly stable current source and an amplifier with a high input impedance to minimize the sensor load.

3.2 Prototype Specifications

The geometric specification for the prototypes is targeted to match the material sample variability with respect to size and shape in the production process of electrical devices. Given the fact that material samples show a remanent magnetic field up to 20 mT, one design requirement is to establish a minimum flux density of $B_{\min} = 100$ mT inside the material samples. This requirement makes a sufficiently high magnetization current necessary which potentially leads to thermal issues in terms of overheating. For this reason a thermal analysis is performed and a maximum measurement duration is specified. The resulting design parameters including the geometric and electric specification are summarized in Tab. 3.1. A geometric model of the magnetic circuit is depicted in Fig. 3.2.

Parameter Name	Parameter Symbol	Value	Unit
min. Distance between poles	l_{pole}	38	mm
min. Air Gap Size	l_{air}	1	mm
min. Core thickness	d_{core}	10	mm
Core Relative Permeability	$\mu_{\mathrm{r,core}}$	5000	-
Copper Wire Diameter	d_{wire}	0.96	mm
max. Wire Current	$I_{\max}$	3.6	A
Wire Current	I_{wire}	3	A
max. Coil Thickness	d_{coil}	11	mm
min. Flux Density	$B_{\min}$	100	mT
max. Time Span	$\Delta t_{\max}$	300	s

Tab. 3.1: Prototype design parameters.
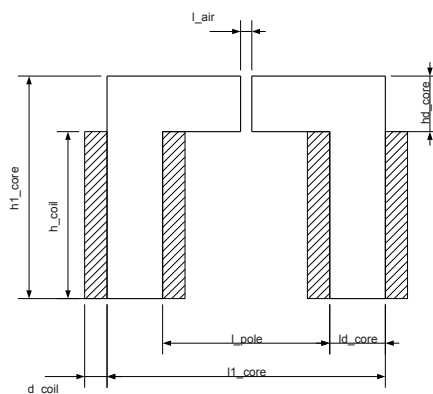
Fig. 3.2: Prototype core and coil with dimensions.

The geometric specification and the requirement of a minimum flux density are the starting point for the dimensioning of the magnetization coils.

3.3 Magnetic System Design

In order to achieve a minimum magnetic flux density $B_{\text{min}} = 100\,\text{mT}$ along the material sample, a minimum magnetomotive force

$$\Theta_{\text{min}} = \sum_i H_i \cdot l_i = H_{\text{core}} \cdot l_{\text{core}} + H_{\text{air}} \cdot l_{\text{air}} + H_{\text{pole}} \cdot l_{\text{pole}} \tag{3.1}$$

is required in the magnetic circuit. Considering that the core permeability is several orders of magnitude larger than the permeability of the material sample, this term can be simplified by neglecting the magnetomotive force in the core

$$\Theta_{\text{min}} \approx H_{\text{air}} \cdot l_{\text{air}} + H_{\text{pole}} \cdot l_{\text{pole}}. \tag{3.2}$$

Plugging in the minimum required flux density gives the magnetic field of

$$H_{\text{pole}} = \frac{B_{\text{min}}}{\mu_0} = \frac{100\,\text{mT}}{4\pi \cdot 10^{-7}\,\text{Vs/Am}} = 80000\,\text{A/m} \tag{3.3}$$

$$H_{\text{air}} = H_{\text{pole}} = 80000\,\text{A/m} \tag{3.4}$$

for the pole and air gap, respectively. Finally by considering a certain stray field, this results in a required magnetomotive force

$$\Theta_{\text{min}} \approx 80000\,\text{A/m} \cdot 0.038\,\text{m} + 80000\,\text{A/m} \cdot 0.001\,\text{m} = 3120\,\text{A} \overset{\text{stray field}}{\approx} 3200\,\text{A}. \tag{3.5}$$

Given the maximum magnetization current, this can be used to determine the parameters of the magnetization coils, in particular the number of coil turns N and the resulting coil height h_{coil} according to Equ. 3.6 to Equ. 3.10.

$$N_{\text{2coils}} = \frac{\Theta}{I_{\text{wire}}} = \frac{3200\,\text{A}}{3\,\text{A}} \approx 1066 \tag{3.6}$$

$$N_{\text{coil}} = \frac{N_{\text{2coils}}}{2} = \frac{1066}{2} \approx 530 \tag{3.7}$$

To accommodate the required coil turns, a layered coil setup is chosen. The total number of required layers can be determined from maximum thickness (determined by the core geometry) and the wire diameter d_{wire} as

$$N_{\text{coil,layers}} = \frac{d_{\text{coil}}}{d_{\text{wire}}} = \frac{11\,\text{mm}}{0.96\,\text{mm}} \approx 11 \tag{3.8}$$

Consequently, this results in a total of

$$N_{\text{coil,layer}} = \frac{N_{\text{coil}}}{N_{\text{coil,layers}}} \approx 48 \tag{3.9}$$

turns per layer and a coil height of

$$h_{\text{coil}} = N_{\text{coil,layer}} \cdot d_{\text{wire}} = 48 \cdot 0.96\,\text{mm} \approx 46\,\text{mm}. \tag{3.10}$$

The resulting mean path length is then

$$l_{\mathrm{mean}} = 107 \, \mathrm{mm}. \tag{3.11}$$

and the overall path length is

$$l_{\mathrm{wire}} = N \cdot l_{\mathrm{mean}} = 55.6 \, \mathrm{m}. \tag{3.12}$$

The prototype coil parameters are summarized in Tab. 3.2.

Parameters	Symbol	Value
Length	l_{coil}	46 mm
inner Distance	$l_{\mathrm{coil,i}}$	14 mm
outer Distance	$l_{\mathrm{coil,o}}$	35 mm
Thickness	h_{coil}	11 mm
mean Path Length	l_{mean}	107 mm

Tab. 3.2: Prototype coil dimensions.

The calculated parameters are verified by a simulation using the set parameters and a core geometry described above. The simulation results in Fig. 3.3 indicate that the established design fulfills the requirement in terms of the minimum flux density along the center of the pole.
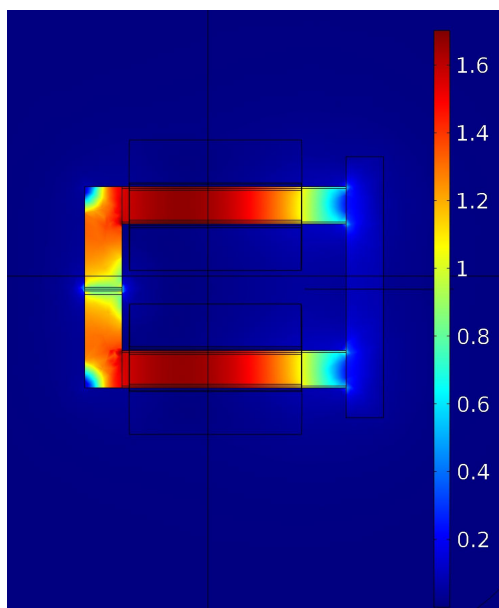
Fig. 3.3: Parameter verification with numeric simulation tool and magnetic flux density B in Tesla.

In the simulation the mean magnetic flux density over the volume of the material sample is $B_{\mathrm{mean}} \approx 0.11$ T.

3.4 Thermal Dimensioning

To investigate on the effects of the high magnetization currents a worst case analysis of the thermal issues [18] is performed. For this purpose the overall energy during a measurement cycle

$$\Delta W_E = P_{\text{coil}} \cdot \Delta t = c \cdot m \cdot \Delta T \tag{3.13}$$

is considered where P_{coil} are the coil losses, Δt is the duration of the measurement cycle, c is the materials specific heat capacity, m is the material mass and ΔT is the resulting temperature change during the measuring cycle.

The coil losses are mainly caused by the ohmic losses which depend on the wire dimension and the material conductivity. The specific material properties for the employed magnetization coil are summarized in Tab. 3.3.

Parameters	Symbol	Value
Diameter	d_{wire}	$0.96\,\text{mm}$
Density	ρ_{copper}	$8920\,\text{kg/m}^3$
Coil Mass	m_{coil}	$0.375\,\text{kg}$
Specific Heat Capacity	c_{copper}	$385\,\text{J/kg/K}$
Specific Conductivity	σ	$58.1 \cdot 10^6\,\text{S/m}$
Maximum Current Density	$J_{\text{wire},5}$	$5\,\text{A/mm}^2$

Tab. 3.3: Copper wire parameters.

Considering the particular material properties and the coil dimensions, the losses can be computed as

$$P_{\text{coil}} = I^2 \cdot R_{\text{wire}} = I^2 \cdot \frac{l_{\text{wire}}}{\sigma \cdot A_{\text{wire}}}. \tag{3.14}$$

Finally, the maximum temperature rise during the measurement cycle can be computed by rearranging Equ. 3.13

$$\Delta T = \frac{P_{\text{coil}} \cdot \Delta t}{c_{\text{copper}} \cdot m_{\text{coil}}} = \frac{17.1\,\text{W} \cdot 300\,\text{s}}{385\,\text{J/kg/K} \cdot 0.375\,\text{kg}} = 35\,\text{K} \tag{3.15}$$

This means that during the measurement cycle $\Delta t = 300\,\text{s}$, the maximum temperature rise is $\Delta T = 35\,\text{K}$ which lies within a reasonable range considering the thermal specification of the wire insulation.

3.4.1 Simulation

To further back up the analytical considerations regarding the thermal behavior, a simulation is performed for the specified measurement duration. For this purpose, the coil

is abstracted as a solid copper block, where the spacing between the individual wires is considered by means of a filling factor

$$F = \frac{d_{\text{wire}}^2 \cdot \frac{\pi}{4} \cdot N_{\text{max}}}{h_{\text{coil}} \cdot l_{\text{coil}}} = \frac{(0.96 \text{ mm})^2 \cdot \frac{\pi}{4} \cdot 520}{46 \text{ mm} \cdot 10.5 \text{ mm}} \approx 0.78 \tag{3.16}$$

which is a commonly used approach for orthocyclic coils. The resulting simulation model is shown in Fig. 3.4a. The equivalent required total current $I_{coil,tot}$ can be determined using the filling factor as

$$I_{\text{coil,tot}} = I_{\text{max}} \cdot N_{\text{max}} \cdot k = 3.6 \text{ mm} \cdot 520 \cdot (1 + (1 - F)) = 2283 \text{ A} \tag{3.17}$$

and is inserted to the copper block.
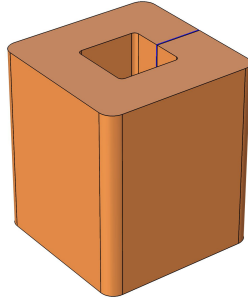
(a) Adiabatic heating 3D simulation model.
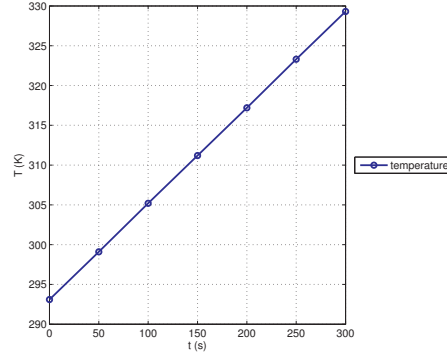
(b) Adiabatic heating 3D simulation temperature plot.

Fig. 3.4: The Adiabatic heating 3D simulation with geometric model and results.

Fig. 3.4b present the temperature rise along the defined time span Δt_{max} starting at $293.1 \text{ K} \approx 20 °\text{C}$. The maximum temperature rise during the measurement cycle is $\Delta T \approx 36 \text{ K}$ which agrees with the theoretic analysis. For this reason, no further considerations regarding the thermal behavior need to be carried out since the temperature change lies within the specifications of the insulation material.

3.5 Electronic Circuits

To measure the magnetic flux B, a Hall sensor of type HE144 is employed. This sensor requires a highly stable current source and a low impedance output amplifier. The individual circuit elements are described in the following paragraphs.

3.5.1 Hall Sensor Current Source

To provide a stable source current, a discrete current source LM134 [14] is used. The schematic circuit layout featuring a temperature compensation is shown in Fig. 3.5a. The positive temperature coefficient of the actual current source circuit is compensated by means of a standard diode having a negative temperature coefficient. For a proper compensation, the resistor values R_1 and R_2 need to be determined depending on the used source current I_{Set}.
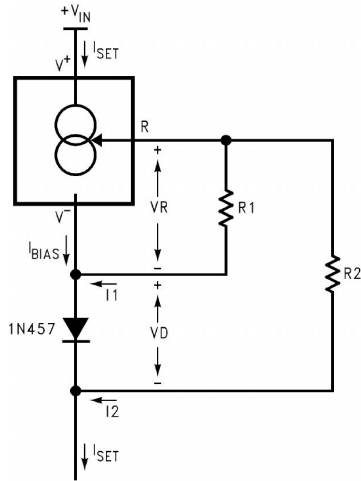
(a) LM134 with temperature compensation circuit.
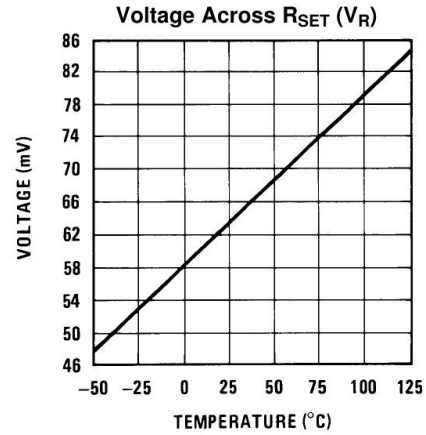
(b) Voltage across $R_{Set}(V_R)$

Fig. 3.5: LM134 current source. LM134 with temperature compensation circuit and the set voltage V_R over temperature.

To achieve a low signal-to-noise ratio, the supply current is chosen to be $I_{\text{Set}} = 1\,\text{mA}$ according to the datasheet specification. The individual temperature coefficients of the LM134 with about $+0.23\,\text{mV/°C}$ and the silicon diode in flow direction with about $-2.1\,\text{mV/°C}$ are the starting point for dimensioning the two resistors.

$$I_{\text{Set}} = I_1 + I_2 \tag{3.18}$$

$$\frac{dI_{\text{Set}}}{dT} = \frac{dI_1}{d_T} + \frac{dI_2}{d_T} \approx \frac{230\,\mu\text{V/°C}}{R_1} + \frac{230\,\mu\text{V/°C} - 2.1\,\text{mV/°C}}{R_2} \tag{3.19}$$

$$= 0 \text{ (solved for a temperature coefficient of 0)}$$

$$\frac{R_2}{R_1} \approx \frac{2.1\,\text{mV/°C} - 230\,\mu\text{V/°C}}{230\,\mu\text{V/°C}} \approx 8.13 \tag{3.20}$$

The calculation takes the forward voltage of the diode with approximately $0.6\,\text{V}$ and a set voltage $V_R = 64\,\text{mV}$ @ $25\,°\text{C}$ which is obtained from Fig. 3.5b. The LM314 datasheet

shows that the bias current I_{Bias} contributes to the voltage drop V_R at a share of 5.9%.

$$I_{\text{Set}} = I_1 + I_2 + I_{\text{Bias}}$$
$$= \frac{V_R \cdot 1.059}{R_1} + \frac{V_R \cdot 1.059 + V_D}{R_2}$$
$$\approx= \frac{67.7\,\text{mV}}{R_1} + \frac{67.7\,\text{mV} + 0.688\,\text{V}}{8.13 \cdot R_1}$$
$$I_{\text{Set}} \approx \frac{0.161\,\text{V}}{R_1}$$

Plugging in the chosen source current value of $I_{\text{Set}} = 1\,\text{mA}$ gives following values for R_1 and R_2:

$$I_{\text{Set}} \approx 1\,\text{mA} = \frac{0.161}{R_1} \tag{3.21}$$

$$R_1 = 161\,\Omega \tag{3.22}$$

$$R_2 = 8.13 \cdot R_1 = 1306\Omega \tag{3.23}$$

For the implementation, the resistors are chosen according to the E96 resistor series with the values $R_1 = 160\,\Omega$ and $R_2 = 1300\,\Omega$.

3.5.2 Hall Sensor Output Signal Amplifier

The low-magnitude output voltage of the LM314 Hall-Sensor is amplified using a LTC2053 instrumentation amplifier which provides a common mode rejection ratio (CMMR) of 116 dB. This ensures that the current load to the Hall sensor is kept at a minimum in order to avoid any signal distortions. The additionally required circuitry consists only of two external resistors which define the gain factor G.

3.6 Reference Measurements

In this section the BH-curves of three chosen material samples are measured using a commercially available measurement system (*MagMess* [15] and a *F.W.Bell* tesla meter [16]). The three samples consist of stain less steel 1.4301 [1] with low, medium and high relative permeability. The initial categorization is performed using the established inspection approach using a permanent magnet as described in Chapter 1.

3.6.1 Measurement Setup

Fig. 3.6 sketches the measurement setup consisting of a electro magnet and a Hall sensor as well as the material sample between the two poles. The electro magnet provides a

homogeneous magnetic field.
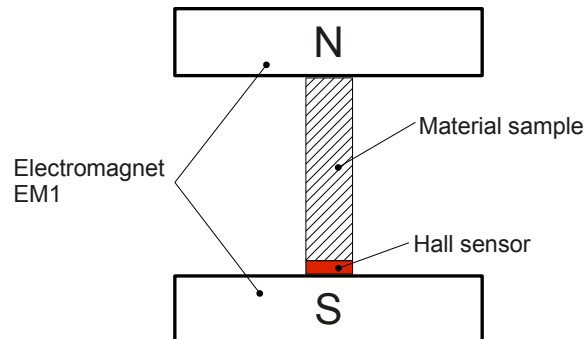
Fig. 3.6: BH-curve evaluation measurement setup. Electro magnet with material sample under test and calibrated Hall sensor.

During the measurement sequence the magnetization current is increased in small steps. At each step the Hall sensor value and the magnetization current is recorded. The BH-curve is obtained by two measurement runs at the same pole distance. In the first sequence no material sample is present and with the measured magnetic flux density B values the magnet field H can be calculated. The second test run is done with a material sample. The combination of both test runs provides specific BH-curve of the material. The measurement results for the three different material samples are summarized in Tab. 3.4 and visualized in Fig. 3.7.

Tab. 3.4 presents the results from the measurements for the different material samples.

Low Magnetic		medium Magnetic		High Magnetic	
H_{low}	B_{low}	H_{med}	B_{med}	H_{high}	B_{high}
A/m	T	A/m	T	A/m	T
8355.6	0.0118	8371.6	0.013	8276.1	0.0232
16552	0.023	15852	0.0228	16385	0.0448
24828	0.034	23571	0.034	24009	0.0647
32706	0.0445	32181	0.0453	32110	0.0818
40982	0.0555	40226	0.0566	40990	0.0987
50213	0.0669	49060	0.066	49386	0.1138
58330	0.0785	58330	0.0832	58012	0.12915
67243	0.0895	67243	0.0942	66765	0.14475
76394	0.1008	76394	0.1059	75360	0.15866
84989	0.1124	84989	0.1166	84273	0.17278
130190	0.1695	130190	0.1742	130030	0.24063
175230	0.2264	175230	0.2328	174270	0.3029
218920	0.2823	218920	0.2875	218280	0.36315
261010	0.3347	261010	0.3396	259260	0.4173
301200	0.3858	301200	0.3902	299050	0.4693
339000	0.4332	339000	0.4367	337010	0.5166

Tab. 3.4: BH-curve reference measurement results. The BH-curves for the three chosen samples.

(a) BH-curves from the sample material with air as reference.

(b) Material samples μ_r-Curves as a function of H.
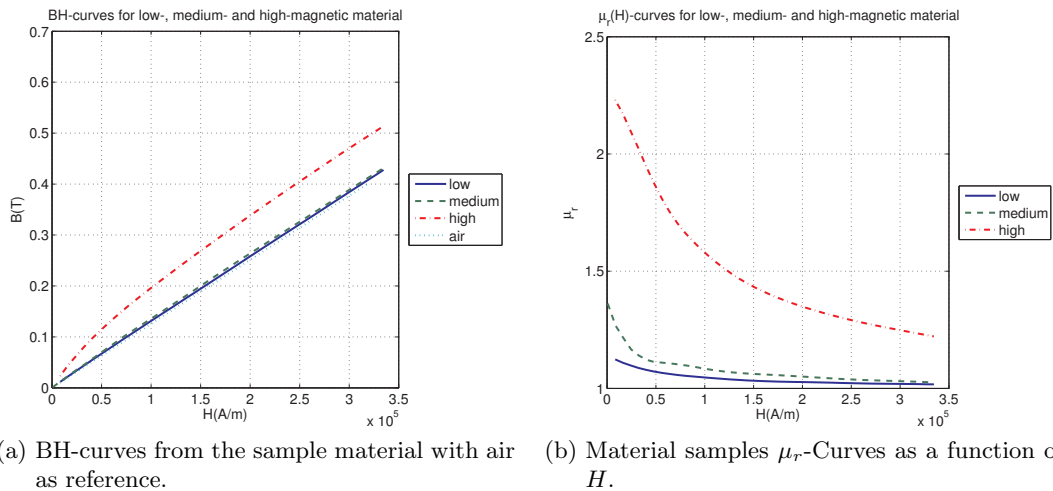
Fig. 3.7: Reference BH-curves and μ_rH-curves of the chosen materials with low, medium and high relative magnetic permeability.

Although the three samples consist of steel 1.4301 [1] with a stated relative permeability of $\mu_r \leq 1.3$ they show a considerable variation in their relative permeability. This highlights the importance of a reliable quality inspection for production processes. The

currently established inspection mechanism only allow for a rough categorization but do not provide a quantitative measure.

The conducted reference measurements build the base line for the evaluation of the presented permeability sensor which is evaluated in detail in the next chapter.

4 Prototype Verification and Measurements

This chapter presents measurements done for the verification of the prototypes A, B and C defined in the design part in Chapter 3. First, the automated measurement setup used in all measurements is presented and a reliable calibration method is developed. Second, the prototypes A, B and C get characterized based on an equal measurement and the dependency on the sample material thickness is investigated using Prototype A and B. Third, a statistical investigation and some sensitivity measurements are done on Prototype A. Finally, all material samples get measured and an investigation to estimate the relative permeability is done.

4.1 Measurement Setup

The used mechanical prototype from Fig. 4.1 are build according to the parameters defined in Sec. 3.2. In Fig. 4.1 the prototype with the attached magnetic short on the open side of the U-core can be seen. In Fig. 4.2 the measurement setup is illustrated in more detail.
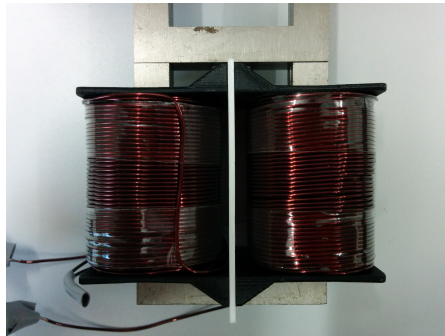
Fig. 4.1: The physical setup of Prototype A showing the core and the two magnetization coils.

The sketch in Fig. 4.2 illustrated the automated test setup. The notebook controls the magnetization current and measures the Hall sensor values. A detailed description of the used devices is listed in Tab. 4.1.
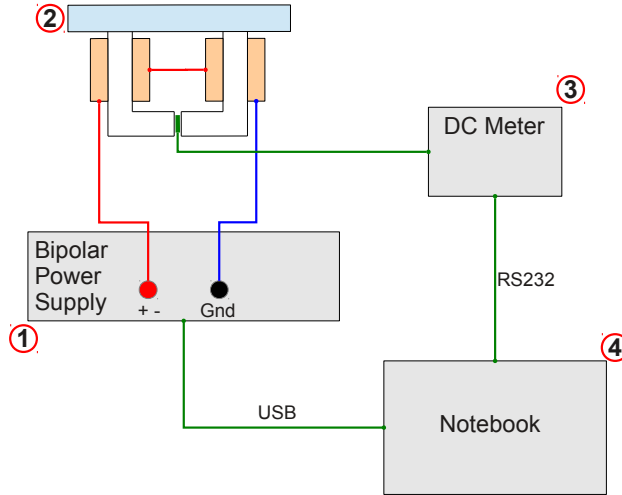
Fig. 4.2: Sketch of the measurement setup used in all experiments.

Device Nr.	Device Name	Details
1	Hameg HM8143	Biploar Power Supply 2A Sink/Source with USB Connection
2	Prototype Sensor	Prototype Sensor with Material Sample
3	HP 34401A	Digital Multimeter with RS232 Connection
4	Notebook	Device Interface and Measurement Controller

Tab. 4.1: List of devices used in the measurement setup.

4.2 Prototype Calibration

The output of the Hall sensor is determined by a gain factor S_{Hall}, a linearity factor L_{Hall} and an additional offset parameter O_{Hall}. The goal of the calibration procedure is to determine this sensor parameters using a calibrated reference. In particular, this section establishes the underlying sensor model and describes a reference measurement to determine the individual parameters for a given setup. In addition, the calibration is carried out for different temperature values to investigate on the impact of changing environmental conditions.

The scaling parameter S_{Hall} is determined using an initial reference measurement where the Hall sensor is replaced by a reference resistor with $R_{\mathrm{Hall}} = 1000\,\Omega$, which lies in the magnitude of the Hall sensor internal resistance.

Parameters	Symbol	Value
Ref. Resistor	R_{Hall}	$1000\,\Omega$
Resistor Voltage	V_{R}	$1.02\,\text{V}$
Resistor Current	I_{R}	$1.02\,\text{mA}$

Tab. 4.2: Current source values.

According to the data sheet the Hall sensor HE144 [17] delivers a Hall voltage $V_{\text{N,Hall}}$ of about $100\,\text{mV}$ at a magnetic flux density $B_{\text{N,Hall}} = 0.1\,\text{T}$ and a nominal supply current of $I_{\text{N,Hall}} = 5\,\text{mA}$. By suppling the Hall sensor with a smaller current the Hall voltage has to be scaled according to the nominal supply current $I_{\text{N,Hall}}$ and the used current I_{R} as described in Equ. (4.1).

$$S_{\text{Hall}} = \frac{I_{\text{N,Hall}} \cdot B_{\text{N,Hall}}}{I_{\text{R}} \cdot V_{\text{N,Hall}}} = \frac{5\,\text{mA} \cdot 0.1\,\text{T}}{1.02\,\text{mA} \cdot 0.1\,\text{V}} = 4.902\,\text{T/V} \tag{4.1}$$

Parameters	Symbol	Unit
Nominal Supply Current	$I_{\text{N,Hall}}$	A
Nominal Flux Density	$B_{\text{N,Hall}}$	T
Nominal Hall Voltage	$V_{\text{N,Hall}}$	V
Supply Current	I_{R}	A

Tab. 4.3: Hall sensor parameters.

According to the Hall sensor manual [17] the sensor has a linearity factor $L_{\text{Hall}} \leq 1$. The two point calibration can adapt this linearity and offset error of the signal. To get one equation to calibrate the Hall sensor the gain parameter is included. The gain is calculated with Equ. 4.1. The two point calibration is done with the raw Hall sensor values $s_1(I, B)$ and $s_2(I, B)$ amplified by the gain S_{Hall}.
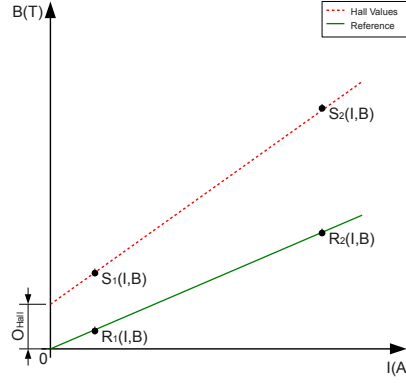
Fig. 4.3: The two point calibration example scheme illustrates the reference curve and the curve for calibration.

Parameter	Symbol	Unit
Hall Voltage Scaling	S_{Hall}	T/V
Linearity Scaling	L_{Hall}	-
Offset Compensation	O_{Hall}	T

Tab. 4.4: Two point calibration and gain parameters.

The gain of the Hall sensor S_{Hall} is calculated in Equ. (4.1). The two parameters needed by the two point calibration can be calculated with Equ. (4.2) to Equ. (4.6). This three parameters are listed in Tab. 4.4.

The raw Hall sensor values $s(I, B)$ are amplified by the gain S_{Hall} as input to the two point calibration.

$$S_1(I, B) = S_{\mathrm{Hall}} \cdot s_1(I, B) \tag{4.2}$$
$$S_2(I, B) = S_{\mathrm{Hall}} \cdot s_2(I, B) \tag{4.3}$$

When the current $I = 0$ the Hall sensor offset S_{Off} depicted in Fig. 4.3 is determined.

$$O_{\mathrm{Hall}} = S(I, B)|_{I=0} \tag{4.4}$$

The linearity scaling factor is determined by four known points. In this case $R_1(I, B)$ and $S_1(I, B)$ at $I = 0$ to get the offset S_{Off} at the same time and $R_2(I, B)$ and $S_2(I, B)$ at $I \neq 0$.

$$S_1(I, B) \cdot L_{\mathrm{Hall}} - R_1(I, B) = S_2(I, B) \cdot L_{\mathrm{Hall}} - R_2(I, B) \tag{4.5}$$
$$L_{\mathrm{Hall}} = \frac{R_2(I, B) - R_1(I, B)}{S_2(I, B) - S_1(I, B)} \tag{4.6}$$

The resulting Hall sensor value can be calculated from the raw Hall sensor value with Equ. (4.7).

$$B_{\text{Hall}} = (V_{\text{Hall}} \cdot S_{\text{Hall}} - O_{\text{Hall}}) \cdot L_{\text{Hall}} \tag{4.7}$$

4.2.1 Calibration Reference

To establish well defined conditions the idea is to shorten the U-shaped prototype core with a piece of core material which almost eliminates the magnetic stray field. A sketch of the shorted calibration core is illustrated in Fig. 4.4. The magnetic flux density in the air gap is measured with a calibrated tesla meter [16]. The calibrated probe was used in Sec. 3.6 at the *University of Graz Physical Institute*. This measured values are listed in Tab. 4.5 and build the calibration reference.
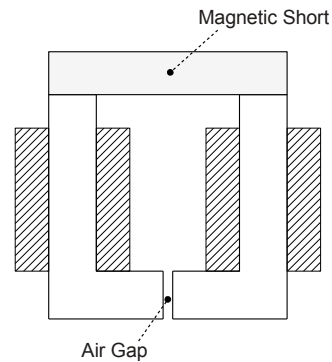
Fig. 4.4: Magnetic shorted prototype as calibration reference.

Nr.	mag. Current	Flux Density
	A	T
1	0.000	−0.020
2	0.15	0.120
3	0.196	0.1585
4	0.500	0.462
5	0.712	0.597
6	1.000	0.682
7	0.714	0.614
8	0.494	0.474
9	0.185	0.195
10	0.100	0.099
11	0.000	0.000

Tab. 4.5: Shorted prototype core calibration reference values.

4.2.2 Calibration Sequence

The reference values from the calibration listed in Tab. 4.5 are used to adapt the uncalibrated values delivered from the Hall sensor HE144. The three calibration parameters used in Equ. (4.7) and their values are stated in Tab. 4.6.

(a) Hall sensor values without linearity and   (b) The calibrated Hall sensor values offset calibration.   matches the underlying referenc.
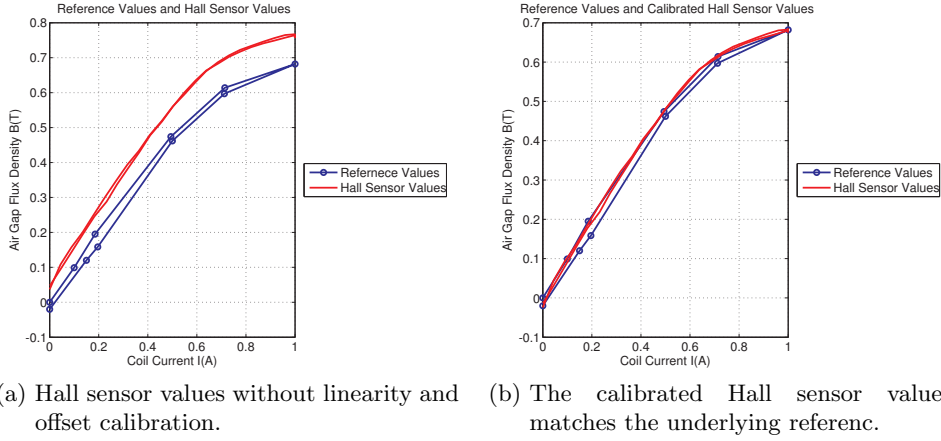
Fig. 4.5: Hall sensor calibration. In Fig. 4.5a the results after the gain calibration and in Fig. 4.5b after the complete calibration can be seen.

Parameter S_{Hall} is calculated with Equ. (4.1). The parameters L_{Hall} and O_{Hall} are calculated from a two point calibration described before.

Parameter	Symbol	Value
Hall Voltage Scaling	S_{Hall}	4.902 T/V
Linearity Scaling	L_{Hall}	0.968
Offset Compensation	O_{Hall}	62 mT

Tab. 4.6: Hall sensor calibration values. The three calibration parameters to the measurement from Fig. 4.5

Fig.4.5 presents the calibration results which show an nearly identically shape. The three calculated calibration values are listed in Tab.4.6.

4.2.3 Temperature Dependency and Calibration at different Temperatures

Due to the fact that a Hall sensor has a high sensitivity to temperature changes it requires a calibration at different temperatures. At first the already known two point

calibration is tested. The temperature dependency of the Hall sensor values were tested by suppling the prototype magnetization coils with a current of 2 A where the prototype was in a box to achieve a faster heating. In Fig. 4.6 the temperature dependency of the measured Hall sensor values can be seen.
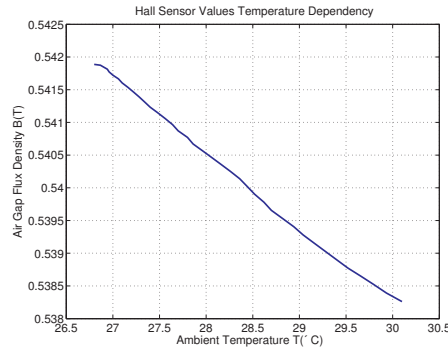
Fig. 4.6: Temperature dependency of the Hall sensor.

The values from Fig. 4.6 result in a temperature coefficient of $k_{\mathrm{T,Hall}} = -1.25\,\mathrm{mT/K}$ at the sensor.

Two temperature calibrations at 26°C and 32°C are presented in Fig. 4.7a and Fig. 4.7b. The calibration parameters used at the different temperature are listed in Tab. 4.7.

(a) The calibrated Hall sensor values at 26 °C and calibration reference values.

(b) The calibrated Hall sensor values at 32 °C and calibration reference values.
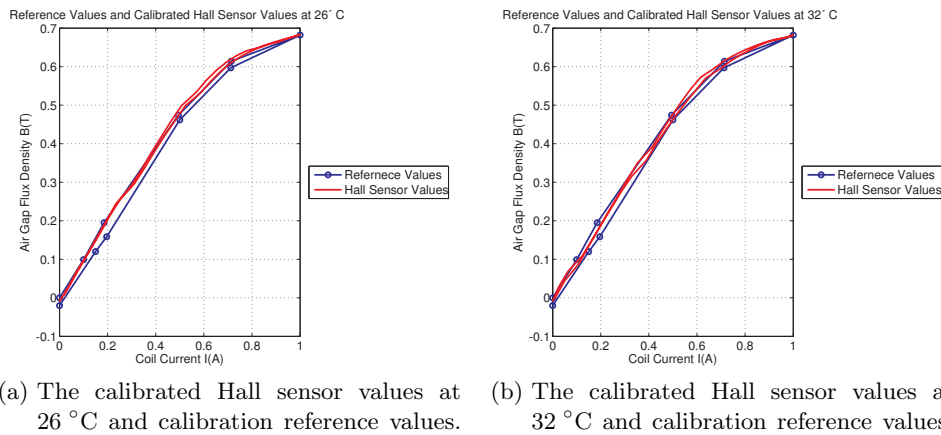
Fig. 4.7: Hall sensor temperature calibration at two different temperatures.

Parameter	Symbol	Value at 26 °C	Value at 32 °C
Hall Voltage Scaling	S_{Hall}	4.902 T/V	4.902 T/V
Linearity Scaling	L_{Hall}	0.965	0.986
Offset Compensation	O_{Hall}	63 mT	71 mT

Tab. 4.7: Temperature dependent Hall sensor calibration values. Calibration values at 26 °C and 32 °C.

The results from the calibration measurement at 26 °C and 32 °C in Fig. 4.7a and 4.7b validate that it is possible to calibrate the sensor at different temperatures. Without a temperature information the calibration is restricted to constant temperatures and has to be done at the beginning of a new measurement sequence.

The simple calibration model with three parameters is a suitable method to fit the Hall sensor values to the calibration reference. An additional advantage is that in case of a defect Hall sensor the sensor can be replaced without a new reference calibration.

4.3 Material Samples

The measurements are done with a set of provided material samples. All material samples are numbered and categorized by means of the the currently established quality inspection. The different material samples are shown in Fig. 4.8 and Tab. 4.8 lists the corresponding categorization results.

(a) Material Samples P1…P10

(b) Material Samples P11…P14
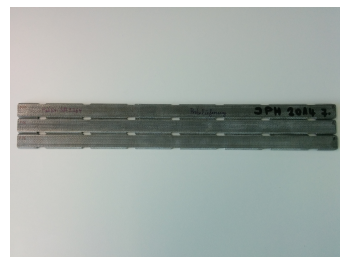
(c) Material Samples P15…P17
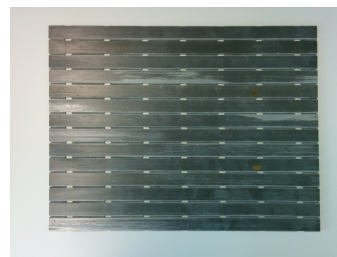
(d) Material Samples P18…P31

(e) Material Samples P32…P35

(f) Material Samples P36…P39

Fig. 4.8: Material samples P1 …P39 used during the measurements.

	Magnetic Categorization by Quality Inspection			
Sample Number	Non Mag.	Low Mag.	Medium Mag	High Mag.
P1	x			
P2			x	
P3				x
P4	x			
P5			x	
P6	x			
P7				x
P8	x			
P9			x	
P10			x	
P11				x
P12				x
P13				x
P14				x
P15				x
P16				x
P17				x
P18				x
P19				x
P20				x
P21				x
P22				x
P23				x
P24				x
P25				x
P26				x
P27				x
P28				x
P29				x
P30				x
P32			x	
P33	x			
P34		x		
P35	x			
P36		x		
P37		x		
P38				x
P39	x			

Tab. 4.8: Measurement samples and categorization (non magnetic, low, medium and high relative permeability) based on the standard quality inspection mechanism.

4.4 Basic Prototype Characterization

In order to compare the prototypes A, B and C all three prototypes are used in the defined calibration and measurement sequence using the material samples **P1**, **P2** and **P3**. In Fig. 4.9 and Fig. 4.10 the physical prototypes setups are presented. Prototype B and C are identical except for the current direction and the resulting magnetic field which is either perpendicular and tangential through the material sample.
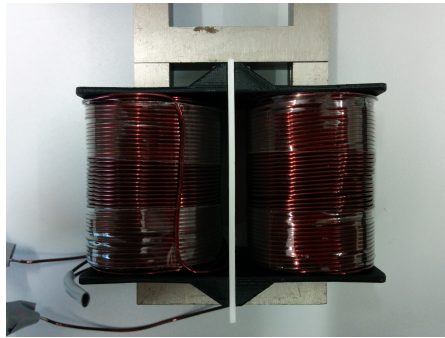
Fig. 4.9: The physical setup of Prototype A showing the core and the two magnetization coils.
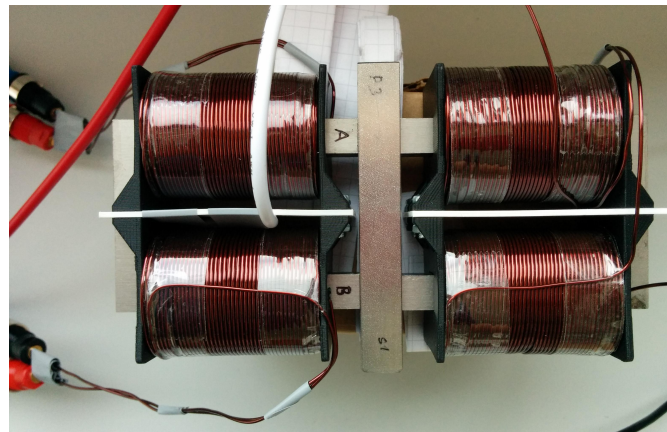
Fig. 4.10: The physical setup of Prototype B and C showing the two U-shaped cores and the four magnetization coils.
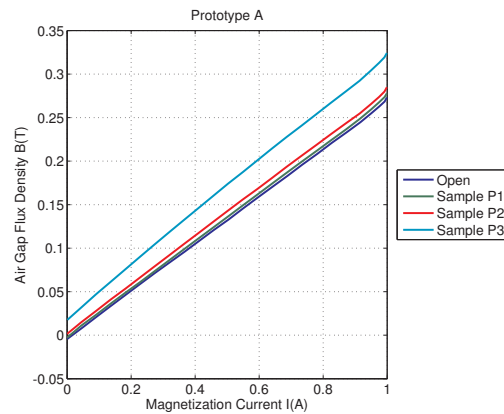
(a) Measurement sequence results Prototype A.
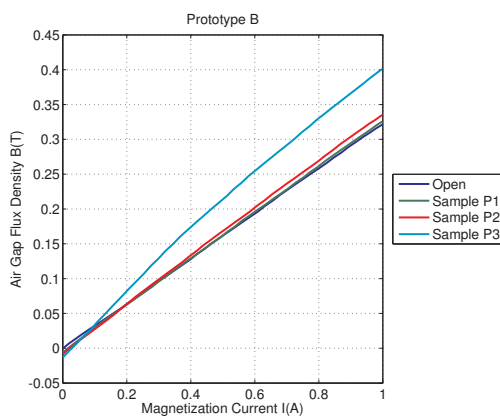
(b) Measurement sequence results Prototype B.
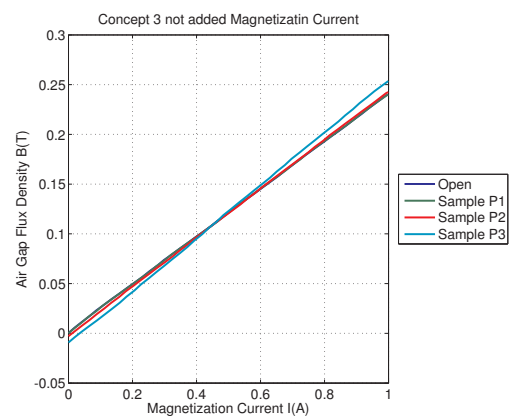
(c) Measurement sequence results Prototype C.

Fig. 4.11: Measurement sequence for comparison of Prototype A, B and C. All prototypes performed the same sequence with material sample **P1**, **P2**, **P3** and air as reference.

The measured magnetic flux density for Prototype A in Fig. 4.11a shows a nearly linear dependence on the magnetization current. Furthermore, the different permeabilities of the material samples lead to a deterministic change in the resulting B-field. In contrast, Prototype B in Fig. 4.11b only shows a piece-wise linear behavior, especially for higher magnetization currents. Prototype C in Fig. 4.11c, however does not provide the desired characteristic and shows a very low sensitivity to the permeability of the material sample. This means that, although Prototype A has a potentially larger stray field, it nevertheless shows a highly linear B-field characteristic and shows the desired sensitivity to the material sample permeability. For this reason, Prototype A is analyzed and evaluated in the subsequent measurements in detail.

4.5 Dependency on Material Sample Geometry

The dependency on the material sample geometry is evaluated in more detail on material samples with a different thickness. The measurements are done on the prototypes A and B.

4.5.1 Prototype A

On Prototype A the measurement is done according to the measurement sequence in Tab. 4.10 with the different material sample thicknesses shown in Tab. 4.9. The samples **P1** to **P3** have a rectangular cross section and therefore a different thickness. The smaller and the bigger thickness are indicated by **P1.1** and **P1.2**, respectively. The material samples **P11** to **P14** are stacked together starting with **P11** and ending with all four samples stacked together.

Sample	Thickness
	mm
P1.1, P2.1, P3.1	10
P1.2, P2.2, P3.2	14
P11-P14	4 ... 16

Tab. 4.9: Thickness of the material samples. The samples **P1** to **P3** have a side with a smaller and one with a bigger thickness. The samples **P11** to **P14** are stacked together adding one sample at each sequence step.

In Fig. 4.12 the results at different thicknesses are presented with one reference measurement at the beginning where no sample is present.
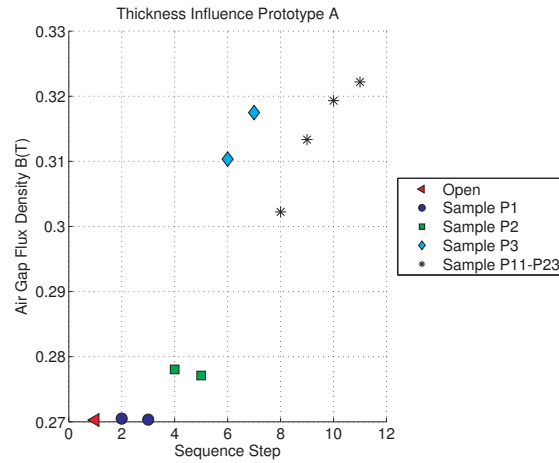
Fig. 4.12: Materials with different thickness on Prototype A. Starting with an initial reference measurement at the beginning.

	Test Sequence							
Sequence Nr.	1	2	3	4	5	6	7	8...11
Material Sample	Non	P1.1	P1.2	P2.1	P2.2	P3.1	P3.2	P11-P14

Tab. 4.10: Test sequence on Prototype A with different material sample thicknesses.

The results in Fig.4.12 indicate that for material samples with a small magnetic permeability the change in the thickness has a negligible influence. Contrary for materials with higher relative permeabilities the change in thickness has a significant influence to the result.

4.5.2 Prototype B

For the measurement on Prototype B the thickness of the material sample **P10**, **P3** and **P35** is shown in Tab. 4.11. For each material sample the distance between the two cores is set to the material thickness. The according measurement sequence is listed in Tab. 4.12.

Sample	Thickness
	mm
P3	4
P10	12
P35	15

Tab. 4.11: Thickness of the material samples.

In Fig. 4.13a the results at different thicknesses are presented with an additional reference measurement where no sample is present. In Fig. 4.13b the non linear change to the distance between the poles is shown.
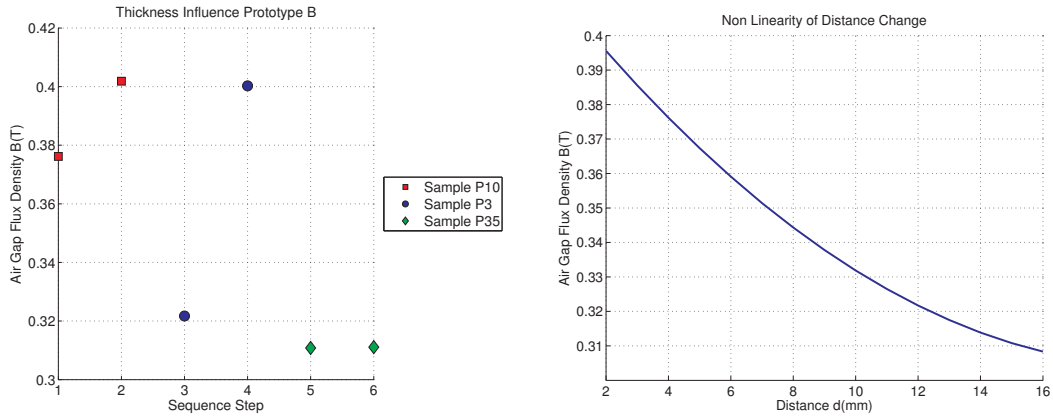
(a) Materials with different thickness on Prototype B. One measurement with and without material sample for each sample is done.

(b) Prototype B non linearity due to distance change between the poles.

Fig. 4.13: Prototype B with different material thickness. Measurement results on material samples with different thickness and nonlinearity of distance change between the poles.

	Test Sequence					
Sequence Nr.	1	2	3	4	5	6
Sample Thickness	4 mm	4 mm	12 mm	12 mm	15 mm	15 mm
Material Sample	Non	P10	Non	P3	Non	P35

Tab. 4.12: Test sequence on Prototype B with different material sample thicknesses.

At each distance change between the poles a new reference measurement has to be done. Due to the non linear behavior of the distance change the measurement is only stable and comparable when the material samples have the same thickness.

4.6 Statistical Evaluation

In this experiment the measurement reproducibility for different magnetization currents is investigated in more detail. For this purpose an experiment is performed as discussed below.

In the first experiment, the flux density is measured in the air gap at different magnetization currents with a set of material samples. The magnetization current is set to 0 A, 0.5 A and 1 A and the procedure is repeated 50 times to obtain a total of $M = 150$ measurements. The measurements are conducted with material sample **P3**, without a material sample and with a shorted magnetic core as shown in Fig. 4.4. The individual measurement results for each magnetization current and material sample are shown in Fig. 4.14.
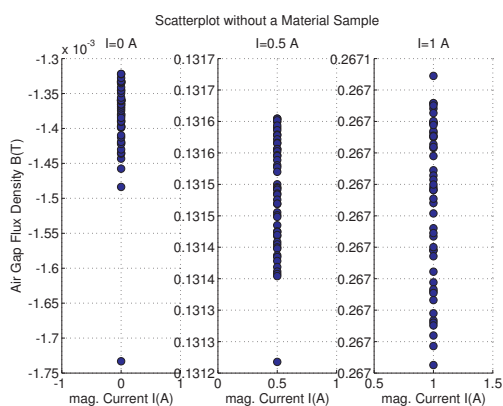
(a) Measurement result distribution when no sample is present and a magnetization current of 0 A, 0.5 A and 1 A.
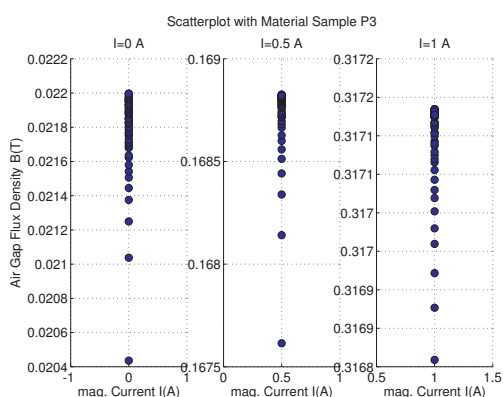
(b) Measurement result distribution with material sample **P3** and a magnetization current of 0 A, 0.5 A and 1 A.
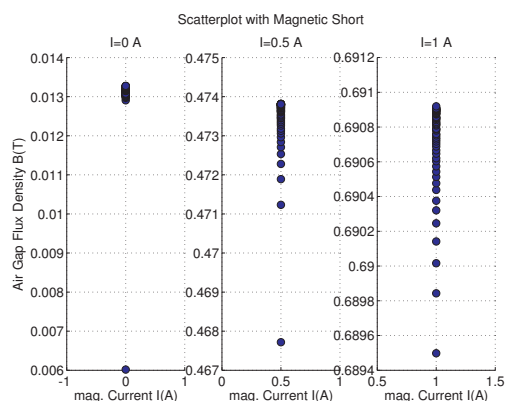
(c) Measurement result distribution with shorted magnetic core and a magnetization current of 0 A, 0.5 A and 1 A.

Fig. 4.14: Deviation on repeated measurement results. The deviation on repeated measurements at different magnetization currents and different material samples is shown.

The scatter plots in Fig. 4.14 show a very small deviation except for a single outlier in each measurement. This outlier is the result from the initial magnetization of the

material sample. The deviation value depends on the hysteresis curve of the material and the prototype core. The values in Tab. 4.13 to Tab. 4.15 state the mean B_μ, minimal $B_{\min}$, maximal $B_{\max}$, difference $\Delta B_{\min}$ and standard deviation B_σ values for the listed material sample at each magnetization current.

| Magnetization Current I | Open Core | | | | |
| | $B_{\min}$ | $B_{\max}$ | $\Delta B_{\min}$ | B_μ | B_σ |
A	mT	mT	mT	mT	mT
0.00	-1.73	-1.32	0.41	-1.38	0.06
0.50	131.27	131.65	0.39	131.53	0.09
1.00	266.96	267.05	0.09	267.01	0.03

Tab. 4.13: Results with open core.

| Magnetization Current I | Material Sample P3 | | | | |
| | $B_{\min}$ | $B_{\max}$ | $\Delta B_{\min}$ | B_μ | B_σ |
A	mT	mT	mT	mT	mT
0.00	20.44	22.00	1.56	21.76	0.28
0.50	167.61	168.83	1.21	168.72	0.21
1.00	316.86	317.18	0.33	317.14	0.03

Tab. 4.14: Results with material sample P3.

| Magnetization Current I | Magnetic Shorted Core | | | | |
| | $B_{\min}$ | $B_{\max}$ | $\Delta B_{\min}$ | B_μ | B_σ |
A	mT	mT	mT	mT	mT
0.00	6.02	13.28	7.26	13.00	1.01
0.50	467.72	473.82	6.10	473.34	0.97
1.00	689.50	690.92	1.42	690.68	0.30

Tab. 4.15: Results with magnetic shorted core.

Especially for small relative permeabilities, the results in Tab. 4.13 to Tab. 4.15 show a small variance which highlights that the measurement principle yields highly reproducible and reliable measurements.

4.7 Sensitivity to Material Sample Placement

To investigate on the sensitivity regarding the placement of the sample material, the previous experiment is extended in the following way. For each measurement, the material sample is manually re-inserted into the measurement setup. For this experiment, the two material samples **P1** (low permeability) and **P3** (high permeability) are used.

Fig. 4.15a and Fig. 4.15b show the measurement sequence with no magnetization current and a magnetization current of 1 A, respectively. The actual measurement sequence is listed in Tab. 4.16.

(a) Lift off repeatability at 0 A.   (b) Lift off repeatability at 1 A.
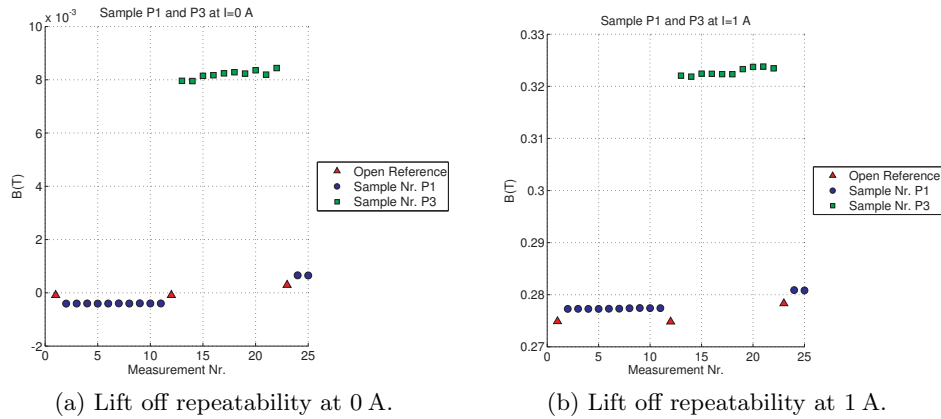
Fig. 4.15: Lift of repeatability at different magnetization currents and test runs.

	Test Sequence					
Sequence Nr.	1	2...11	12	13...22	23	24...25
Material Sample	Non	P1	Non	P3	Non	P1

Tab. 4.16: Test sequence with non stationary material sample.

The measurement results from Fig. 4.15a and Fig. 4.15b show that a material sample with a high remanence affects the value of the core remanence and thus leads to offset changes in the subsequent measurements. Besides this effect, the measurements do not show a significant dependence on the material placements. The remanence effect can be mitigated by resetting the magnetization current for each new measurement.

4.8 Sensitivity to a Non Flat Surface

This experiment investigates on the sensitivity to a non flat surface of a material sample. This is done by increasing the air gap between the core poles and the material sample. The increasing air gap is simulated by multiple spacing elements. Tab. 4.17 lists the layer thickness and flux density results in the air gap at a magnetization current of 0.5 A. Fig. 4.16 presents the results for a magnetization current of 0...1 A and the zoomed results at 0.5 A.

(a) Influence of a non flat surface with material sample P3.

(b) Detail view at a magnetization current of 0.5 A.
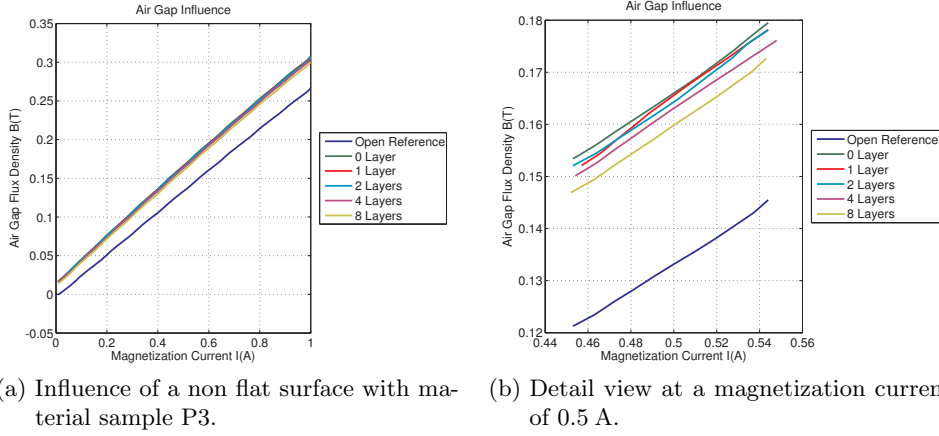
Fig. 4.16: Non flat surface influence. Multiple layers of spacing elements simulate the dependency to a non flat surface. The detail view illustrates that with more layers the flux density in the air gap decreases.

Sample	Layers	Air Gap	Air Gap Flux Density	abs. Deviation	rel. Deviation
		mm	T	mT	%
No Sample	0	0	0.133	-	-
Sample **P3**	0	0	0.166	33	-
Sample **P3**	1	0.2	0.165	32	3
Sample **P3**	2	0.4	0.164	31	6
Sample **P3**	4	0.8	0.163	30	9
Sample **P3**	8	1.6	0.160	27	18

Tab. 4.17: Non flat surface influence. Multiple layers of spacing elements simulate the dependency to a non flat surface.

The resulting air gap size is the sum of both air gaps at the poles. The change in the measured values listed in Tab. 4.17 has a maximum deviation of 6 mT. The deviation in % is calculated as follows. The difference between the magnetic flux density with no material sample and sample P3 is assumed as the 100 %. This gives a maximum deviation of about about 18 % as calculated in Equ. (4.8) to Equ. (4.10).

$$\Delta B_{100} = B_{\text{P3,no gap}} - B_{\text{No}} = 0.166\,\text{T} - 0.133\,\text{T} = 33\,\text{mT} \tag{4.8}$$

$$\Delta B_{\text{max}} = B_{\text{P3,no gap}} - B_{\text{P3,max gap}} = 0.166\,\text{T} - 0.160\,\text{T} = 6\,\text{mT} \tag{4.9}$$

$$d_{\text{max}} = \frac{\Delta B_{\text{max}} \cdot 100\,\%}{\Delta B_{100}} = \frac{6\,\text{mT} \cdot 100\,\%}{33\,\text{mT}} = 18.2\,\% \tag{4.10}$$

ΔB_{100} is the difference without sample and with sample taken as 100 %. ΔB_{max} is the difference with sample at no air gap and maximum air gap. d_{max} is the deviation in % at maximum air gap.

Considering the requirements in practical production processes and the surfaces of the different material samples, the air gap size is typically below 0.4 mm. According to the calculated values in Tab. 4.17 an air gap of up to 0.4 mm results in a measurement error of maximum 6 %. This means that even material samples with non-flat surfaces can be characterized with a sufficient accuracy.

4.9 Sensitivity to the Material Sample Orientation

In this experiment the sensitivity to orientation changes of the material sample is evaluated. For this purpose, material sample **P3** is used in a series of repeated measurements. The orientation changes of the sample are carried out according to the test sequence listed in Tab. 4.18. The measurement setup is shown in Fig. 4.17. The red ellipse in the figure indicates the orientation and side. The marked orientation points from the pole **A** to the pole **B** on side 2.
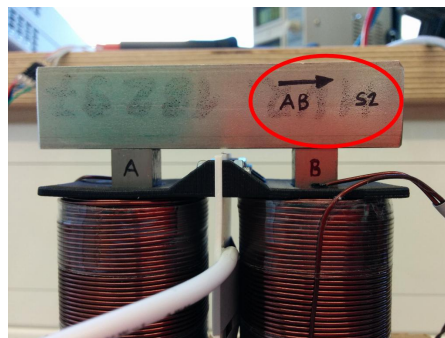
Fig. 4.17: The figure shows the setup for the direction and side change influence and the direction naming **A,B**.

Sequence Nr.	Side	Direction
1	$S1$	A-B
2	$S2$	A-B
3	$S3$	A-B
4	$S4$	A-B
-	-	Switch Orientation
5	$S1$	B-A
6	$S2$	B-A
7	$S3$	B-A
8	$S4$	B-A

Tab. 4.18: Air gap influence

(a) Sample P3 Side 1 in direction **A-B** and **B-A**.

(b) Sample P3 Side 2 in direction **A-B** and **B-A**.

(c) Sample P3 Side 3 in direction **A-B** and **B-A**.

(d) Sample P3 Side 4 in direction **A-B** and **B-A**.
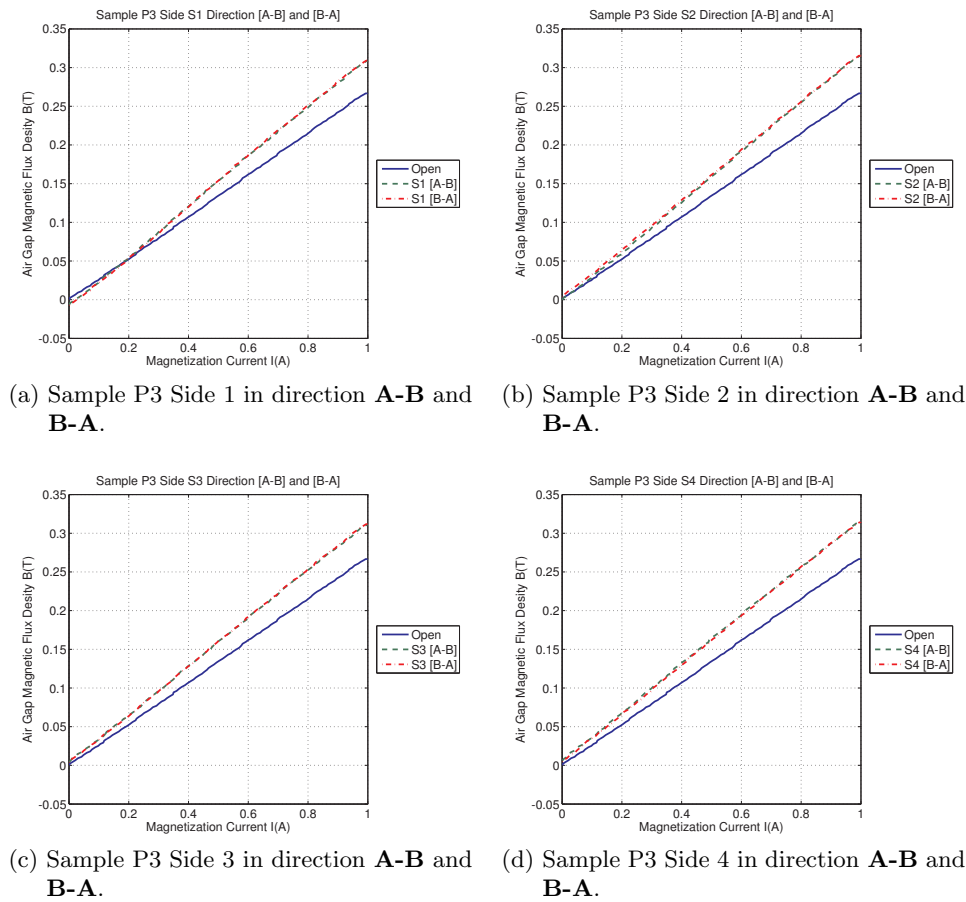
Fig. 4.18: The figure presents the influence to the orientation and side changes of a material.

The resulting measurement curve in Fig. 4.18a shows a certain remanence effect resulting from a previous magnetization. After changing the direction from **A-B** to **B-A** repeatedly shows an opposite remanence. After an initial magnetization to overcome the remanence, the direction change has no influence on the results as shown in Fig. 4.18b to Fig. 4.18d. The initial opposite magnetization can be avoided by repeating the measurement with a sufficiently high magnetization current for each sample.

4.10 Measurement of all Material Samples

In this experiment all material samples **P1 . . . P38** are measured. Fig. 4.19a shows the measurement results without a magnetization current, whereas the results with a magnetization current of 1 A are shown in Fig. 4.19b.

(a) First measurement with no magnetization current.

(b) Second measurement with magnetization current of 1 A.
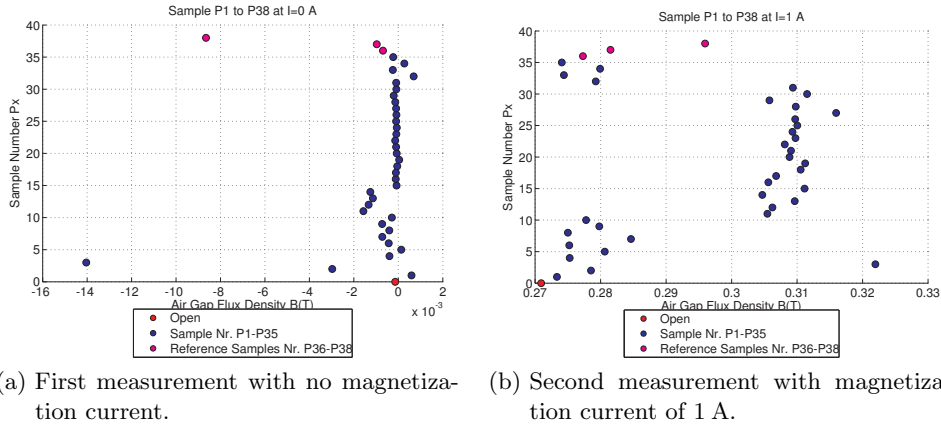
Fig. 4.19: The figures illustrate the influence of the remanence and the different relative permeabilities of each material sample.

In Fig. 4.19a the magnetic remanence of each sample is highlighted. Especially, material sample P3 shows a considerable remanence. In contrast, material samples **P11**...**P35** do not show a significant remanence. In Fig. 4.19, the different samples can be roughly categorized into a total of three clusters having similar material properties. Hence, the material samples **P11**...**P31** consisting of a particular material show nearly the same magnetic properties according to the results in Fig. 4.19a.

The measurements described above show that the presented sensor prototype can be used to determine the B-field changes depending on a particular material sample in an effective and reliable manner. In order to characterize the actual material properties in terms of the relative permeability, the next step is to integrate the reference measurements described in Sec. 3.6. The reference measurements provide a look-up possibility for unknown material samples which can be used to estimate the relative permeability. However, the limited number of reference measurements also limit the resulting measurement range and the available resolution. For this reason, an idea is to integrate simulation results in a bootstrap approach to provide the required range and resolution.

4.11 Relative Permeability Estimation

As an outcome of this work there are four main possibilities to estimate the relative permeability of the sample materials using Prototype A.

- A look-up function $\mu_r = f(B)$ based on the reference materials measured in Chapter 3.

- A look-up function $\mu_r = f(B)$ based on an accurate simulation model.

- The relation between the air gap flux density B_{empty} when no material sample is present and the air gap flux density B_{sample} when a material sample is present.

- A analytic method based on the magnetic equivalent circuit, which is according to the results stated in Chapter 2 not discussed.

4.11.1 Estimation based on Reference Materials

The estimation of the relative magnetic flux density is done with two reference materials **P36** and **P38**. Due to their linear behavior illustrated in Fig. 4.20b the measured B-field and relative permeability values are used to build a linear function

$$\mu_r = f(B). \tag{4.11}$$

The material samples **P1**, **P2** and **P3** depicted in Fig. 4.20a are chosen and their relative permeability is determined in Fig. 4.21b.

(a) Alignment of all material sample values also reference and simulation values at a magnetization current of 1 A.

(b) $\mu_r = f(B)$ lookup function with reference sample **P36** and **P38** as support points.
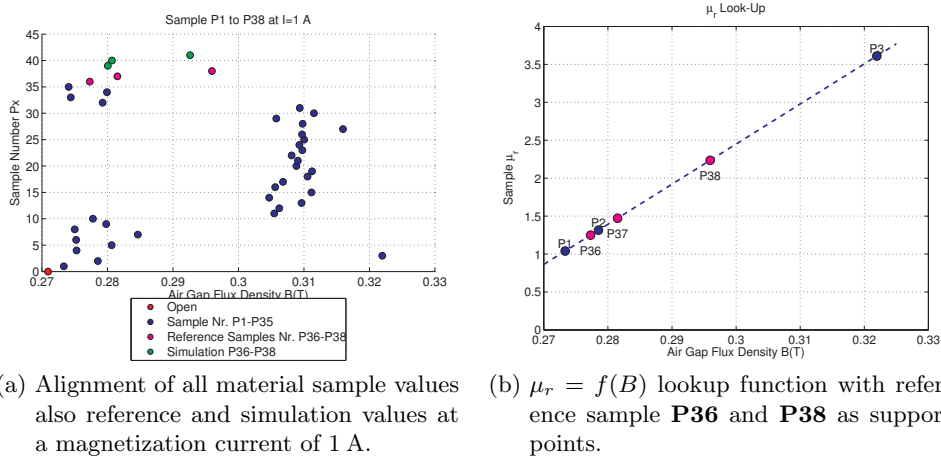
Fig. 4.20: All samples and μ_r-lookup function. All samples including reference samples and simulation results are shown and μ_r-lookup function with support points **P36** and **P38**. The relative permeability of sample **P37** is determined from the interpolation.

The linear look-up function build with the reference samples **P36** and **P38** give a relative permeability of $\mu_r = 1.5$ for the sample **P37** which has a good agreement to the value of $\mu_r = 1.4$ from Sec. 3.6. The relative permeability estimation of a material sample taking reference materials with known relative permeabilities is a good option. But to achieve a high resolution a lot of reference samples are needed.

4.11.2 Estimation based on a Simulation Model

To estimate the relative permeability of a material sample using a simulation a very accurate model has to be provided. Based on this the prototype core is simulated with a defined BH-curve also including the non magnetic glue layers which hold the core metal sheets together. In Fig. 4.21a the simulation values show a good accordance with the reference values and in Fig. 4.21b the look-up function based on simulations results for a relative permeability of $\mu_r = 1 \ldots 6$ is illustrated.

(a) The calibrated simulation values and calibration reference values.

(b) $\mu_r = f(B)$ lookup function with simulation values. **P36**, **P37** and **P38** as validation points.
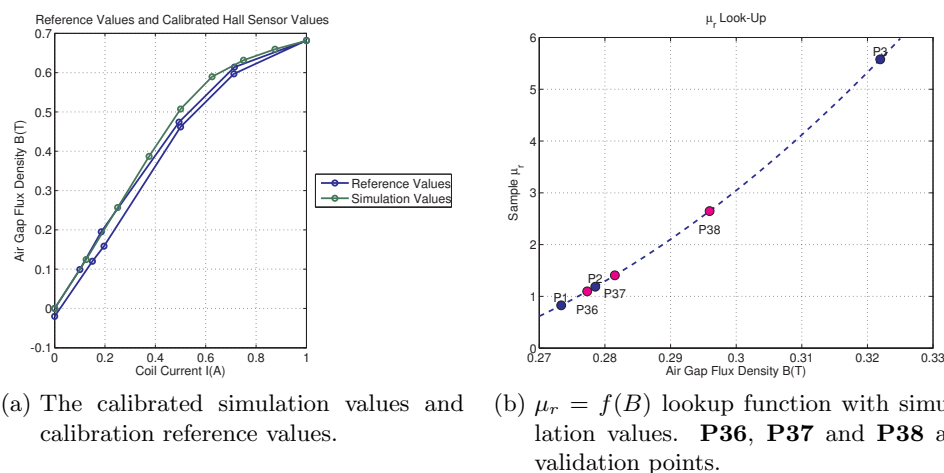
Fig. 4.21: Simulation with Reference and μ_r-lookup function. Simulation values against reference values show good accordance. The look-up function is calculated according to the simulation values.

The relative permeability estimates of the reference samples determined from the look-up function in Fig. 4.21b are listed in Tab.4.19. The estimated relative permeabilities show a good agreement with the values measured in Sec. 3.6.

Material Sample	P36	P37	P38
Estimated μ_r	1.1	1.4	2.6
Reference μ_r	1.1	1.4	2.2

Tab. 4.19: Estimated relative permeability and reference relative permeability of the sample materials.

The resolution and range of the look-up function based on the simulation is adaptable and show a non linear trend. The look-up function shows some problems at small values where a relative permeability $\mu_r < 1$ is calculated which is not possible for steels. The estimation by taking the simulation as a reference needs well measured material BH-curves

and an exact defined simulation model to avoid problems like a relative permeability of steel below one.

4.12 Estimation based on the Ratio between Different Air Gap Flux Densities

The estimation based on the flux density in the air gap needs a reference measurement B_{empty} where no sample is present and a measurement with sample B_{sample}. Both measurement are evaluated over the full range of the magnetization current from $0 \ldots 1\mathrm{A}$. The estimation of $\mu_{\mathrm{r,sample}}$ is calculated according to Equ. 4.12.

$$\mu_{\mathrm{r,sample}} = \frac{B_{\mathrm{sample}}}{B_{\mathrm{empty}}} \tag{4.12}$$

Fig. 4.22a shows the measured values over the full range of the magnetization current and in Fig. 4.22b the estimation results $\mu_{r,sample}$ are depicted.
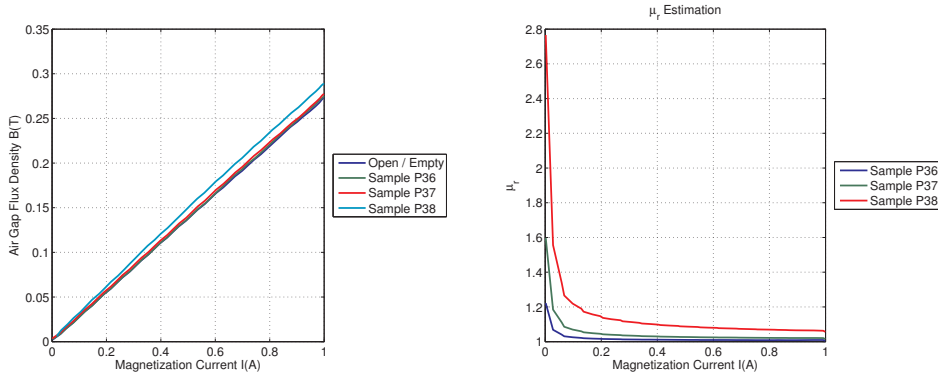
(a) The measurements for the open reference and the material samples over the full magnetization current range.

(b) $\mu_r = f(I)$ calculated with a open reference measurement and the measurements with **P36**, **P37** and **P38**.

Fig. 4.22: $\mu_r = f(I)$ based on two measurements, a reference measurement and a material sample measurement.

The estimation based on the measurements of an empty reference and a material sample show a good agreement to the measured values in Sec. 3.6. The results can't be compared with a BH-curve because the magnetic field in the material sample is not measured explicit.

A possibility to calculate the magnetic field in the probe is using the magnetic circuit theory in Sec. 2.1. The influence of the core can be neglected due to the high permeability

of the core material.The magnetic field H_{sample} in the probe is calculated according to Equ. 4.13 with the magnetization current $N \cdot I$, the measured magnetic flux density B_{gap} in the air gap with length l_{gap} and a mean sample length l_{sample}.

$$N \cdot I \approx \frac{B_{\text{gap}}}{\mu_0} \cdot l_{\text{gap}} + H_{\text{sample}} \cdot l_{\text{sample}} \tag{4.13}$$

(a) Reference measurements of the material samples μ_r as a function of H.

(b) Estimated μ_r values against the calculated magnetic field H.
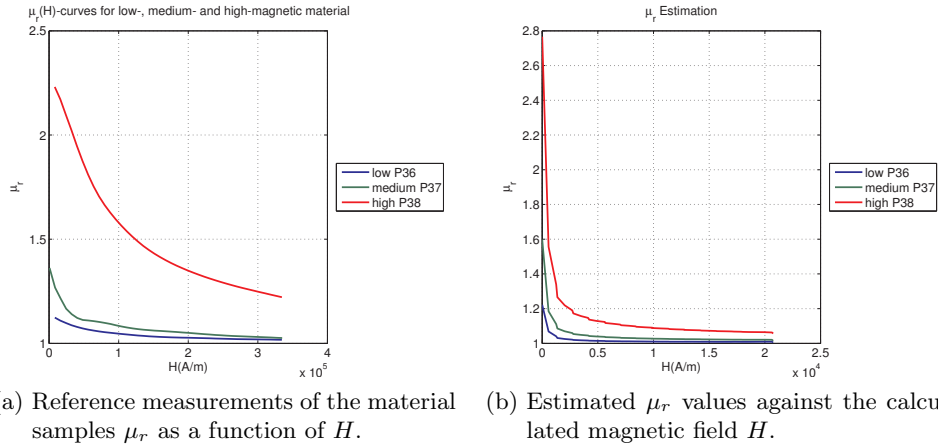
Fig. 4.23: Comparison of the $\mu_r = f(H)$ reference and estimate curves.

The comparison of the reference values in Fig. 4.23a and the estimated values in Fig. 4.23b show comparable results at the beginning but different behaviors afterwards. According to this differences and the fact that the measurement is not done direct at the material sample the determination of the material sample BH-curve is not possible.

5 Final Conclusion and Further Work

The material properties of steels used for the construction and assembly of electrical motors play a crucial role for the resulting efficiency and the overall device performance. Unfortunately, the magnetic material properties, especially the relative permeability shows a considerable variance even across a specific material batch. For this reason, a quality inspection process is required which allows to identify outliers (i.e. materials with significantly different magnetic properties) in an effective way. Currently established quality inspection processes typically rely on the use of a permanent magnet to perform a test whether a material shows a weak or strong magnetization. However, this test performs rather a classification than an actual measurement and is prone to subjective judgment.

The measurement device presented in this thesis aims to improve on this aspect by providing an efficient and reliable way to characterize the magnetic properties of material samples in a production process. For this purpose, a magnetic circuit and a B-field sensor are employed in a guided measurement method. In particular, the magnetic circuit establishes a well defined magnetic flux density which is then altered by the presence of a material sample. In addition to the sensor design, this thesis presents a mathematical sensor model and an adequate calibration strategy. By means of an initial reference measurement and a bootstrap integration of simulation data, the measured B-field changes can be used to determine the relative material permeability.

The sensor design is validated in a series of simulations and experiments regarding measurement reproducibility, sensitivity to different material geometries and material orientation. The conducted simulations and measurements provide consistent results also under practical conditions. The presented approach to integrate reference measurement and simulation data allows for a more general characterization compared to the rather binary inspection processes that are used today. The work presented in this thesis therefore provides an important building block for the quality inspection of electrical devices in order to optimize the resulting efficiency and performance.

In further works some improvements can be done to reach better results from the relative permeability estimation. First, increase the number of reference materials in order to create a more accurate look-up function. Second, fine tuning of the simulation model. Third, create a core calibration references with higher resolution to improve the calibration process. Fourth, include a temperature measurement at the Hall sensor for automatic temperature compensation.

6 Appendix

The appendix includes some parts in more detail and delivers additional information.

6.1 User Guide

The User Guide describes how a measurement cycle depicted in Fig. 6.1 is done from the calibration to the material sample measurement and the result calculation.

6.1.1 Calibration

The calibration is done placing the magnetic short on the measurement device as depicted in Fig. 6.1a and Fig. 6.1b. Two measurements are done at a magnetization current $I = 0\,\text{A}$ and $I = 1\,\text{A}$. These measurements deliver the calibration points $V_{\text{cal},0}$ and $V_{\text{cal},1}$. After the calibration is done the magnetization current is switched off and the magnetic short is removed.

6.1.2 Measurement

Three measurements are done to calculate the magnetic remanence and the relative permeability of the material sample.

- The first measurement $V_{\text{empty},0}$ is done without a material sample according to Fig. 6.1c and a magnetization current of $I = 0$ A.

- The second measurement $V_{\text{sample},0}$ is done with material sample according to Fig. 6.1d and with a magnetization current of $I = 0$ A.

- The third measurement $V_{\text{sample},1}$ is done according to Fig. 6.1e and with a magnetization current of $I = 1$ A.

With the first $V_{\text{empty},0}$ and the second $V_{\text{sample},0}$ measurement result the magnetic remanence $B_{\text{sample,rem}}$ and with the third $V_{\text{sample},1}$ measurement result the relative permeability $\mu_{\text{r,sample}}$ of the material sample is calculated using Equ. 6.1 to Equ. 6.7. If more than one material sample is measured between each measurement the magnetization current must be switched off.

6.1.3 Calculation

The five measured values $V_{\text{cal},0}$, $V_{\text{cal},1}$, $V_{\text{empty},0}$, $V_{\text{sample},0}$ and $V_{\text{sample},1}$ are inserted in a calculation scheme which has as output the remanence $B_{\text{sample,rem}}$ and the estimated relative permeability $\mu_{\text{r,sample}}$ from the look-up function f_{lup} of the material sample. Below a calculation for one measurement is shown.

With the calibration values the offset and linearity parameters are calculated.

$$O_{\text{Hall}} = V_{\text{cal},0} - V_{\text{ref},0} \tag{6.1}$$

$$L_{\text{Hall}} = \frac{R_{\text{ref},1} - R_{\text{ref},0}}{B_{\text{cal},1} - B_{\text{cal},0}} \tag{6.2}$$

With the calibration parameters the real measured relative flux densities are calculated.

$$B_{\text{empty},0} = (V_{\text{empty},0} - O_{\text{Hall}}) \cdot L_{\text{Hall}} \tag{6.3}$$

$$B_{\text{sample},0} = (V_{\text{sample},0} - O_{\text{Hall}}) \cdot L_{\text{Hall}} \tag{6.4}$$

$$B_{\text{sample},1} = (V_{\text{sample},1} - O_{\text{Hall}}) \cdot L_{\text{Hall}} \tag{6.5}$$

With the calculated relative flux density values the material sample magnetic remanence and relative permeability is determined.

$$B_{\text{sample,rem}} = |B_{\text{sample},0} - B_{\text{empty},0}| \tag{6.6}$$

$$\mu_{\text{r,sample}} = f_{\text{lup}}(B_{\text{sample},1}) \tag{6.7}$$
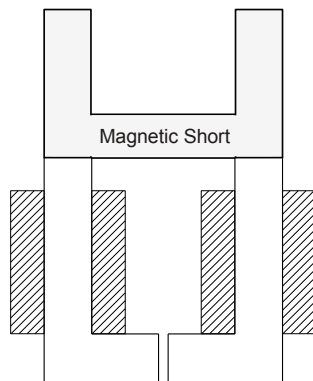
(a) Calibartion meaurement $V_{\mathrm{cal},0}$, Magnetization current $I = 0\,\mathrm{A}$.
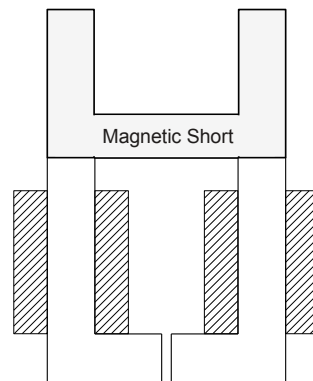
(b) Calibartion meaurement $V_{\mathrm{cal},1}$, Magnetization current $I = 1\,\mathrm{A}$.
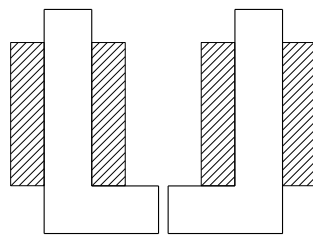
(c) Remanence meaurement $V_{\mathrm{empty},0}$, Magnetization current $I = 0\,\mathrm{A}$.
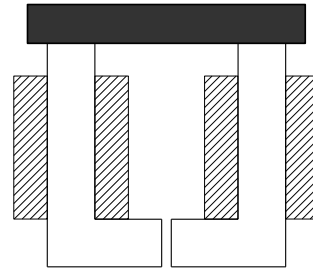
(d) Remanence meaurement $V_{\mathrm{sample},0}$, Magnetization current $I = 0\,\mathrm{A}$.
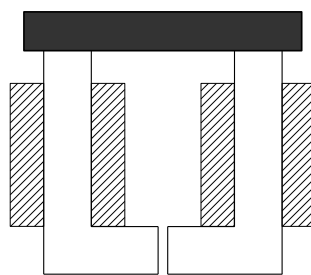
(e) Relative permeability meaurement $V_{\mathrm{sample},1}$, Magnetization current $I = 1\,\mathrm{A}$.

Fig. 6.1: Illustration of the measurement cycle described in the User Guide.

Bibliography

[1] Deutsche Edelstahlwerke, Deutsche Edelstahlwerke GMBH, Auesstraße 4, 58452 Witten. *Steel 14301*, 03 2008.

[2] J.P. Gourber. A Portable Device to Measure Low Magnetic Permeability in Situ. *eConf*, C720919:773, 1972.

[3] Byung-Chill Woo, Kwon sang Ryu, and Young-Eon Ihm. Low- mu; measurement using a special waveform of the magnetizing field. *IEEE Transactions on Magnetics*, 35(5):3748–3750, 1999.

[4] S. Sgobba. Physics and measurements of magnetic materials. *CERN-2010-004*, 4:39–63, 2011.

[5] INSTITUT DR. FOERSTER GmbH & Co. KG, In Laisen 70, 72766 REUTLIN-GEN. *MAGNETOSCOP 1.069*, 05 2008.

[6] I.D. Adewale and Gui Yun Tian. Decoupling the Influence of Permeability and Conductivity in Pulsed Eddy-Current Measurements. *IEEE Transactions on Magnetics*, 49(3):1119–1127, 2013.

[7] Yu Yating, Du pingan, and Yang Tuo. Investigation on contribution of conductivity and permeability on electrical runout problem of eddy current displacement sensor. In *In Proceedings of the IEEE Instrumentation and Measurement Technology Conference (I2MTC) 2011*, pages 1–5, 2011.

[8] R S Davis. New method to measure magnetic susceptibility. *Measurement Science and Technology*, 4(2):141, 1993.

[9] ASTM International. ASTM A341/A341M-00 Standard Test Methods for Direct Current Magnetic Properties of Materials Using D-C Permeameters and the Ballistic Test Methods, 2011.

[10] ASTM International. ASTM A342/A342M-99 Standard Test Methods for Permeability of Feebly Magnetic Materials, 1999.

[11] ASTM International. ASTM A343 Standard Test Method for Alternating-Current

Magnetic Properties of Materials at Power Frequencies Using Wattmeter-Ammeter-Voltmeter Method and 25-cm Epstein Test Frame, 1997.

[12] ASTM International. ASTM A596/A596M-95 Standard Test Methods for Direct-Current Magnetic Properties of Materials Using the Ballistic Method and Ring Specimens, 1999.

[13] COMSOL Inc., New England Executive Park 1, Burlington, USA. *COMSOL Reference Manual*, May 2013.

[14] Texas Instruments, Texas Instruments, Post Office Box 655303, Dallas, Texas 75265. *LM134*, 03 2000.

[15] MagMess, MagMess. Alleestraße 24A, D-44793 Bochum. *MagMess_EM1*, 08 2004.

[16] F.W. BELL, F.W.BELL, 4607SF International Way, Milwaukie OR 97222. *F.W.BELL_7010*, 04 2003.

[17] Hoeben Electronics, Hoeben Electronics, The Netherlands. *HE144*, 11 2011.

[18] Hans Dieter Baehr and Stephan Kabelac. *Thermodynamik Grundlagen und technische Anwendungen*. Springer, Berlin; Heidelberg, 2009.